
Liouville PDE-based sliced-Wasserstein flow

Jayshawn Cooper¹ Pilhwa Lee¹

Abstract

The sliced Wasserstein flow (SWF), a nonparametric and implicit generative gradient flow, is transformed to a Liouville partial differential equation (PDE)-based formalism. First, the stochastic diffusive term from the Fokker-Planck equation-based Monte Carlo is reformulated to Liouville PDE-based transport without the diffusive term, and the involved density estimation is handled by normalizing flows of neural ODE. Next, the computation of the Wasserstein barycenter is approximated by the Liouville PDE-based SWF barycenter with the prescription of Kantorovich potentials for the induced gradient flow to generate its samples. These two efforts show outperforming convergence in training and testing Liouville PDE-based SWF and SWF barycenters with reduced variance. Applying the generative SWF barycenter for fair regression demonstrates competent profiles in the accuracy-fairness Pareto curves.

1. Introduction

We are motivated to transform the uncertainty induced by Monte Carlo sampling to deterministic PDE (mean-field) and to deep learning of normalizing flow (neural ODE). Accordingly, we present an improvement to the sliced Wasserstein flow (SWF) method with its application to fair regression. The main contribution is characterization of the transformation of the Fokker-Planck equation-based approach to a Liouville PDE-based transport with density estimation, thus eliminating the stochastic diffusive term.

More specifically, we introduce a Liouville PDE-based deterministic path sampling method for the sliced Wasserstein flow, which replaces the stochastic elements of the original approach with integration of neural ODE techniques for density estimation within the Liouville PDE framework. This is a new formulation for computing sliced Wasserstein barycenters, based on the superposition of individual Kan-

torovich potentials from empirical distributions specific to each sensitive attribute. The theoretical analysis extends the SWF framework to the gradient flow of barycenter, including a proof of the equivalence of the associated gradient flow to a Fokker-Planck equation.

The paper demonstrates the effectiveness of these improvements through experiments on synthetic data and two real-world datasets: Communities and Crime (Redmond & Baveja, 2022), and Health Care Spending Cost (Zink & Rose, 2019). Results show that the Liouville PDE-based SWF achieves better convergence and/or lower variance compared to the vanilla SWF, particularly in high-dimensional settings with a few sensitive attributes. This does address the scalability of algorithmic debiasing and fairness in high-dimensional statistics, overcoming the curse of dimensionality.

Fairness can be formulated essentially in the same framework as causal inference, i.e., independence of the sensitive attributes can be represented by conditional probability and expectation. A central goal of fairness is to ensure that sensitive information does not “unfairly” influence the outcomes. For example, if we wish to estimate and prescribe the health care spending cost, we would like not to unfairly use additional sensitive information such as gender or race. Here, this kind of “gender” or “race” can be sensitive attributes. The simplest and most popular fairness criterion, called demographic parity, requires the expectation of outcome \hat{Y} to not depend on attribute A (Chiappa et al., 2020):

$$\mathbb{E}[\hat{Y}|A = a] = \mathbb{E}[\hat{Y}|A = \bar{a}], \quad \forall a, \bar{a} \in \mathcal{A}. \quad (1)$$

In a similar but stronger criterion, *i.e.*, considering the full shape of the distribution $p(S|A)$, strong demographic parity (SDP) requires statistical independence between S and A , *i.e.*

$$p(S_a) = p(S_{\bar{a}}), \quad \forall a, \bar{a} \in \mathcal{A}, \quad (2)$$

where S_a is the output variable restricted to the group of individuals with sensitive attributes a , and \mathcal{A} is the collection of attributes in the data. In this work, we use the following definition of (strong) Demographic Parity, which was previously used in the context of regression (Agarwal et al., 2019; Jiang et al., 2019; Chiappa et al., 2020; Chzhen et al., 2020):

Definition 1 (Demographic Parity). A prediction (possibly

¹Department of Mathematics, Morgan State University, Baltimore, MD 21251, USA. Correspondence to: Pilhwa Lee <Pilhwa.Lee@morgan.edu>.

randomized) $g : \mathbb{R}^d \times \mathcal{S} \rightarrow \mathbb{R}$ is fair if, for every $s, s' \in \mathcal{S}$

$$\sup_{t \in \mathbb{R}} |\mathbf{P}(g(X, S) \leq t | S = s) - \mathbf{P}(g(X, S) \leq t | S = s')| = 0.$$

where S is the sensitive attribute.

In the problems of classification and regression, this criteria of fairness can be reformulated in optimal transport and Wasserstein distances (Chiappa et al., 2020). The involving main idea is minimizing the efforts in moving the unfair distributions to a common one:

$$p_{\bar{S}} = \arg \min_{p^*} \sum_{a \in \mathcal{A}} p_a \mathcal{W}_2(p_{S_a}, p^*). \quad (3)$$

These are addressed for classification in Wasserstein-1 distance (Jiang et al., 2019) and for regression in Wasserstein-2 distance (Chzhen et al., 2020). Especially, fair regression is rigorously formulated by Wasserstein barycenter (Chzhen et al., 2020; T. Le Gouic, 2020):

Theorem 1 (Chzhen, et al. 2020). *Assume, for each $s \in \mathcal{S}$, that the measure $\nu_{f^*|_s}$ has a density and let $p_s = \mathbb{P}(S = s)$. Then,*

$$\min_{g \text{ is fair}} \mathbb{E}(f^*(X, S) - g(X, S))^2 = \min_{\nu} \sum_{s \in \mathcal{S}} p_s \mathcal{W}_2^2(\nu_{f^*|_s}, \nu).$$

In the formulation of Theorem 1, f^* is the regression function before adjustment for fairness, and $\nu_{f^*|_s}$ is the probability distribution for f^* with the restriction of the sensitive attribute $S = s$.

In this article, we explore the performance of sliced Wasserstein barycenter that was originally incorporated for the transformation of coloring and texture mixture in computer vision (Rabin et al., 2011; Bonneel et al., 2015). Sliced-Wasserstein is the integration of Wasserstein distance from one-dimensional optimal transport (Bonneel et al., 2015) with its topological equivalence to Wasserstein (Nadjahi et al., 2020). This has a competent performance in the kernel methods and generative algorithms (Kolouri et al., 2016; Deshpande et al., 2018). Especially, we take the core framework from sliced-Wasserstein flows (Liutkus et al., 2019). This is based on the connection between implicit generative modeling and optimal transport, a parameter-free algorithm for learning the underlying distributions of complicated datasets and sampling from them. The involving gradient flow is turned to stochastic differential equations.

As a main effort to improve the SWF scheme, the Fokker-Planck equation is transformed to transport map of Liouville PDE. The associated density estimation is trained by the normalizing flow of neural ODE. Shen et al.

(2022) addressed its underlying property of *self-consistency*. Based on the proof of Liutkus et al. (2019), *further applying linearity in derivatives in the calculus of variations*, the formulation for SWF barycenters is also represented by the Fokker-Planck equation with the drift term represented by the total influence from individual Kantorovich potentials (Theorem 3).

The competence of Liouville PDE-based sliced-Wasserstein flows and barycenters are shown in three showcases: 1) generative optimal transport of a probability distribution from source to target, 2) generative optimal transport for barycenter, 3) fair regression analysis of community and crime as well as health care spending cost. As shown in Tables S1 and S2, the Liouville PDE-based sliced-Wasserstein flows provide improved convergence with reduced loss and/or reduced variance. In the high-dimensional distributions around 60 and 120, the accuracy and/or fairness are improved from Liouville-PDE based SWF barycenter in comparison to the vanilla SWF barycenter, and also as a reasonable alternative in comparison to the exact Wasserstein barycenter, where computational complexity exceedingly elevates getting intractable.

2. Related works

2.1. Normalizing flow, neural ODE, density estimation, and transport map

Density estimation is a very important problem in uncertainty quantification (Tabak & Turner, 2013). There have been efforts to transform the Fokker-Planck equation to the Liouville PDE (Nelson, 1967; Chen et al., 2021; Shen et al., 2022; Xu et al., 2023; Boffi & Vanden-Eijnden, 2023; Albergo & Vanden-Eijnden, 2023). There have been some efforts of proving convergence (Cheng et al., 2024). The Liouville PDE and its evolving probability distribution can be further represented by neural ODE (Chen et al., 2018; Grathwohl et al., 2019).

2.2. Computation of Wasserstein barycenter

Agueh & Carlier (2011) addressed the existence of Wasserstein barycenter. However, the actual computation of Wasserstein barycenter is complicated. Among recent efforts to resolve the complexity in computation, the primal and dual formulation with matrix scaling is regularized to compute the barycenters among discrete empirical measures (Cuturi & Doucet, 2014). Based on the algorithm of iterative Bregman Projections, the complexity of approximating the Wasserstein barycenter of m discrete measures or histograms of size n is shown to be mn^2/ϵ^2 . When an approach based on accelerated gradient descent is used, the complexity is proportional to mn^2/ϵ (Kroshnin et al.,

2019). The fixed-support Wasserstein barycenter problem, which consists in computing the Wasserstein barycenter of m discrete probability measures supported on a finite metric space of size n , was shown to be not a minimum-cost flow problem when $m \geq 3$ and $n \geq 3$ (Lin et al., 2020). On dual formulation of optimal transport, bi-level adversarial learning is also applied based on neural optimal transport (Kolesov et al., 2024).

2.3. Fair regression with Wasserstein barycenter

There has been fair classification (Jiang et al., 2019; Agarwal et al., 2018), and fair regression (Berk et al., 2017; Agarwal et al., 2019; Steinberg et al., 2020; Wang et al., 2023). The formalism of optimal transport has been applied for fairness (Chiappa et al., 2020). In regards to fair regression with Wasserstein barycenter, the constraints of fairness have been prescribed as a pre-processor (Chzhen et al., 2020) or a post-processor projecting the optimal solution to fairness \mathcal{W}_2 (T. Le Gouic, 2020). In between with and without fairness, it is also possible to prescribe partial fairness (Chzhen & Schreuder, 2022).

3. Technical Backgrounds

3.1. Optimal transport on Wasserstein spaces

For two probability measures $\mu, \nu \in \mathcal{P}_2(\Omega)$, $\mathcal{P}_2(\Omega) := \{\mu \in \mathcal{P}(\Omega) : \int |x|^2 d\mu < +\infty\}$, the 2-Wasserstein distance is defined as follows:

$$\mathcal{W}_2(\mu, \nu) := \inf_{\gamma \in \mathcal{C}(\mu, \nu)} \left\{ \int_{\Omega \times \Omega} \|x - y\|^2 d\gamma(dx, dy) \right\}^{\frac{1}{2}},$$

where $\mathcal{C}(\mu, \nu)$ is called the set of *transportation plans* and defined as the set of probability measures γ on $\Omega \times \Omega$ satisfying for all $A \in \mathcal{A}$, $\gamma(A \times \Omega) = \mu(A)$ and $\gamma(\Omega \times A) = \nu(A)$, i.e. the marginals of γ coincide with μ and ν . From now on, we will assume that Ω is a compact subset of \mathbb{R}^d .

In the case where Ω is finite, computing the Wasserstein distance between two probability measures turns out to be a linear programming with linear constraints, and has therefore a dual formulation. Since Ω is a Polish space (i.e. a complete and separable metric space), this dual formulation can be generalized as follows (Villani, 2008) [Theorem 5.10]. In the relaxed duality of Kantorovich,

$$\begin{aligned} \mathcal{W}_2(\mu, \nu) &= \sup_{\psi \in L^1(\mu)} \left\{ \int_{\Omega} \psi(x) \mu(dx) + \int_{\Omega} \psi^c(x) \nu(dx) \right\}^{1/2}, \\ \psi^c(y) &\triangleq \inf_{x \in \Omega} \|x - y\|^2 - \psi(x). \end{aligned}$$

Accordingly, the measurable function $T : \Omega \rightarrow \Omega$ is the optimal map from μ to ν :

$$T(x) = x - \nabla \psi(x), \quad (4)$$

where ψ is called the optimal Kantorovich potential. For one-dimensional measures of $\mu, \nu \in \mathcal{P}_2(\mathbb{R})$, we have the following analytic formulation for the Wasserstein distance with the differences of quantiles between μ and ν :

$$W_2(\mu, \nu) = \int_0^1 |F_{\mu}^{-1}(\tau) - F_{\nu}^{-1}(\tau)|^2 d\tau. \quad (5)$$

3.2. Liouville partial differential equations (PDE)

The governing state equation is the following:

$$\dot{x} = f(x, t), \quad (6)$$

which is a first-order nonlinear system. We define the corresponding Liouville operator (Brockett, 2012):

$$\mathcal{L}(\rho, f)(x, t) = \nabla \cdot (f(x, t)\rho(x, t)).$$

The probability density of the state is represented by the Liouville PDE:

$$\left(\frac{\partial \rho}{\partial t} + \mathcal{L}(\rho, f) \right) (x, t) = 0, \quad (7)$$

with the initial probability density $\rho(x, 0) = \rho_0(x)$. Dynamic optimal transport (OT) represents the Wasserstein distance from the viewpoint of dynamical systems. The L^2 -Wasserstein distance can be measured by the dynamic OT with the following formula (Brenier & Benamou, 2000):

$$W(\mu, \nu)_2^2 = \inf_{(p, f)} (t_1 - t_0) \int_{\Omega} \int_{t_0}^{t_1} p(x, t) |f(x, t)|^2 dt dx, \quad (8)$$

where μ and ν are two distributions at timepoints t_0 and t_1 and $f(x, t)$ represents the velocity or drift term at the state x and time t (Eq. 6). The probability distribution $p(x, t)$ is evolved by the Liouville PDE (Eq. 7) with the initial and final distributions prescribed by $p(\cdot, t_0) = \mu$ and $p(\cdot, t_1) = \nu$.

3.3. Sliced Wasserstein

The projection for any direction $\theta \in \mathbb{S}^{d-1}$ and $x \in \mathbb{R}^d$ is the following:

$$\theta^*(x) \triangleq \langle \theta, x \rangle, \quad (9)$$

where $\langle \cdot, \cdot \rangle$ denotes the Euclidean inner-product and $\mathbb{S}^{d-1} \subset \mathbb{R}^d$ denotes the d -dimensional unit sphere. For any measurable function $f : \mathbb{R}^d \rightarrow \mathbb{R}$ and $\zeta \in P(\mathbb{R}^d)$,

$$f_{\#} \zeta(A) = \zeta(f^{-1}(A)).$$

Sliced Wasserstein distance is defined in the following:

$$SW_2(\mu, \nu) \triangleq \int_{\mathbb{S}^{d-1}} W_2(\theta_{\#}^* \mu, \theta_{\#}^* \nu) d\theta. \quad (10)$$

whose time complexity is $\mathcal{O}(N_\theta dn + N_\theta n \log(n))$ with N_θ samples for the Monte Carlo integration on the hypersphere \mathbb{S}^{d-1} and n samples for empirical measures of $\hat{\mu}$ and $\hat{\nu}$. We consider the functional minimization problem on $\mathcal{P}_2(\Omega)$ for implicit generative modeling:

$$\min_{\mu} \{F_\lambda^\nu(\mu) \triangleq \frac{1}{2} \mathcal{SW}_2^2(\mu, \nu) + \lambda \mathcal{H}(\mu)\}, \quad (11)$$

where $\lambda > 0$ is a regularization parameter and \mathcal{H} denotes the negative entropy:

$$\mathcal{H}(\mu) \triangleq \int_{\Omega} \rho(x) \log \rho(x) dx.$$

3.4. Fokker-Planck equation for sliced-Wasserstein

Theorem 2 (Liutkus et al. 2019). *Let ν be a probability measure on $\bar{B}(0, 1)$ with a strictly positive smooth density. Choose a regularization constant $\lambda > 0$ and radius $r > \sqrt{d}$ where d is the data dimension. Assume that $\mu_0 \in P(\bar{B}(0, r))$ is absolutely continuous with respect to the Lebesgue measure with density $\rho_0 \in L^\infty(\bar{B}(0, r))$. There exists a generalized minimizing movement scheme $(\mu_t)_{t \geq 0}$ associated to Eq. (11) and if ρ_t stands for the density of μ_t for all $t \geq 0$, then $(\rho_t)_t$ satisfies the following Fokker-Planck equation:*

$$\frac{\partial \rho_t}{\partial t} = -\nabla \cdot (v_t \rho_t) + \lambda \Delta \rho_t, \quad (12)$$

$$v_t(x) \triangleq v(x, \mu_t) = - \int_{\mathbb{S}^{d-1}} \psi'_{t,\theta}(\langle x, \theta \rangle) \theta d\theta, \quad (13)$$

in a weak sense. Here, Δ denotes the Laplacian operator, $\nabla \cdot$ the divergence operator, and $\psi_{t,\theta}$ denotes the Kantorovich potential between $\theta_{\#}^* \mu_t$ and $\theta_{\#}^* \nu$.

3.5. Fair regression with Wasserstein barycenter

In Theorem 1, if g^* and ν^* solve the l.h.s. and the r.h.s. problems respectively, then $\nu^* = \nu_{g^*}$, and

$$g^*(x, s) = \left(\sum_{s' \in S} p_{s'} Q_{\nu^*|s'} \right) \circ F_{f^*|s}(f^*(x, s)). \quad (14)$$

where $F_{f^*|s}$ and $Q_{\nu^*|s'}$ are the cumulative probability distribution for f^* in terms of the sensitive attribute s and the quantile function for ν^* in terms of the sensitive attribute s' , respectively.

In all experiments, we collect statistics on the test set $\mathcal{T} = \{(X_i, S_i, Y_i)\}_{i=1}^{n_{\text{test}}}$. The empirical mean squared error (MSE) is defined as follows.

Definition 2 (Mean Squared Error in Fair Regression).

$$\text{MSE}(g) = \frac{1}{n_{\text{test}}} \sum_{(X, S, Y) \in \mathcal{T}} (Y - g(X, S))^2. \quad (15)$$

where $g(X, S)$ is from fair regression derived from Wasserstein barycenter. We measure the violation of fairness constraint (Definition 1) via the empirical Kolmogorov-Smirnov (KS) distance as follows:

Definition 3 (Empirical Kolmogorov-Smirnov (KS) distance).

$$\text{KS}(g) = \max_{s, s' \in S} \sup_{t \in \mathbb{R}} \left\| \frac{1}{|\mathcal{T}^s|} \sum_{(X, S, Y) \in \mathcal{T}^s} \mathbf{1}_{g(X, S) \leq t} - \frac{1}{|\mathcal{T}^{s'}|} \sum_{(X, S, Y) \in \mathcal{T}^{s'}} \mathbf{1}_{g(X, S) \leq t} \right\|. \quad (16)$$

4. Liouville PDE-based Sliced Wasserstein

4.1. Transformation of Fokker-Planck equation to neural ODE

The stochastic differential equation and the associated Fokker-Planck equation are the following:

$$dx = f(x, t)dt + \sigma(x, t)dW_t, \quad (17)$$

$$\frac{\partial \rho}{\partial t} + \nabla \cdot (f\rho) - \frac{1}{2} \nabla \cdot (\sigma \sigma^T \nabla \rho) = 0. \quad (18)$$

The Fokker-Planck equation (Eq. 18) can be transformed to Liouville PDE (Eq. 7) when σ is independent of the state:

$$\frac{\partial \rho}{\partial t} + \nabla \cdot \left(\left(f - \frac{1}{2} \sigma \sigma^T \nabla (\log \rho) \right) \rho \right) = 0. \quad (19)$$

Neural ODE is incorporated not only for the adjoint method for backpropagation and computation of gradients of loss functions, but also for the density estimation of ρ (Chen et al., 2018). The entire drift term of Eq. (19) is

$$f^* = f - \frac{1}{2} \sigma \sigma^T \nabla (\log \rho). \quad (20)$$

Accordingly, the Fokker-Planck equation (Eq. 18) is solved by the augmented dynamics of $(x, \log \rho)$:

$$\frac{d}{dt} \begin{bmatrix} x(t) \\ \log \rho(x(t), t) \end{bmatrix} = \begin{bmatrix} f^*(x(t), t) \\ -\nabla \cdot f^*(x(t), t) \end{bmatrix}. \quad (21)$$

4.2. Liouville PDE-based deterministic path sampling

In order to reduce the variance from Monte Carlo approach, the path sampling is transformed to Eq. 21 based on the Liouville PDE (Eq. 19):

$$\begin{aligned} \bar{X}_{k+1}^i &= \bar{X}_k^i + h \tilde{v}_k(\bar{X}_k^i), \\ \tilde{v}_k(\bar{X}_k^i) &\triangleq -(1/N_\theta) \sum_{n=1}^{N_\theta} \psi'_{k, \theta_n}(\langle \theta_n, \bar{X}_k^i \rangle) \theta_n \\ &\quad - \lambda \nabla \log \rho(\bar{X}_k^i, t_k), \\ \log \rho(\bar{X}_{k+1}^i, t_{k+1}) &= \log \rho(\bar{X}_k^i, t_k) - h \nabla \cdot \tilde{v}_k(\bar{X}_k^i). \end{aligned} \quad (22)$$

5. Liouville PDE-based sliced Wasserstein barycenter

The Wasserstein barycenter ν is formulated in the following:

$$\min_{\nu} \sum_{s \in S} p_s \mathcal{W}_2^2(\nu_{f^*|s}, \nu).$$

The key question is whether there comes an acceptable outcome when we approximate the Wasserstein barycenter ν by the sliced Wasserstein barycenter from the following scalable optimization problem:

$$\min_{\nu} \sum_{s \in S} p_s \mathcal{S}\mathcal{W}_2^2(\nu_{f^*|s}, \nu).$$

We consider the functional minimization problem on $\mathcal{P}_2(\Omega)$ with the entropic regularization:

$$\min_{\mu} \{F_{\lambda}^{\{\nu_s\}}(\mu) \triangleq \frac{1}{2} \sum_s p_s \mathcal{S}\mathcal{W}_2^2(\mu, \nu_s) + \lambda \mathcal{H}(\mu)\}. \quad (23)$$

The minimizer of sliced Wasserstein barycenter is obtained by the convergent generative flow influenced by the integration of individual Kantorovich potentials as justified in the following theorem.

Algorithm 1 Liouville PDE-based sliced-Wasserstein barycenter flows

Input: $\mathcal{D} = \{y_{i,s}\}_{1 \leq s \leq N_s}^{1 \leq i \leq P_s}, \mu_0, N, N_{\theta}, h, \lambda$
Output: $\{\bar{X}_K^i\}_{i=1}^N$
 $\bar{X}_0^i \sim \mu_0$, i.i.d.
 $\theta_n \sim$ from \mathbb{S}^{d-1}
for $\theta \in \{\theta_n\}_{n=1}^{N_{\theta}}$ **do**
 for $s = 1, \dots, N_s$ **do**
 $F_{\theta_{\#}^* \nu_s}^{-1} = \text{QF}\{(\theta, y_{i,s})\}_{i=1}^{P_s}$
 end for
end for
for $k = 0, \dots, K-1$ **do**
 for $\theta \in \{\theta_n\}_{n=1}^{N_{\theta}}$ **do**
 $F_{\theta_{\#}^* \bar{\mu}_{kh}^N} = \text{CDF}\{(\theta, \bar{X}_k^i)\}_{i=1}^N$
 end for
 $\tilde{v}_k(\bar{X}_k^i) = -\frac{1}{N_{\theta}} \sum_{n=1}^{N_{\theta}} \sum_{s \in S} p_s \psi'_{s,k,\theta_n}(\langle \theta_n, \bar{X}_k^i \rangle) \theta_n$
 $-\lambda \nabla \log \rho(\bar{X}_k^i, t_k)$
 $\bar{X}_{k+1}^i = \bar{X}_k^i + h \tilde{v}_k(\bar{X}_k^i)$
 Update the density $\log \rho(\cdot, t_k)$ from Eq. (21).
end for

5.1. Fokker-Planck equation for sliced-Wasserstein barycenter

Theorem 3. *Let ν be a probability measure on $\bar{B}(0, 1)$ with a strictly positive smooth density. Choose a regularization constant $\lambda > 0$ and radius $r > \sqrt{d}$ where d is the data*

dimension. Assume that $\mu_0 \in P(\bar{B}(0, r))$ is absolutely continuous with respect to the Lebesgue measure with density $\rho_0 \in L^{\infty}(\bar{B}(0, r))$. There exists a generalized minimizing movement scheme $(\mu_t)_{t \geq 0}$ associated with Eq. (23) and if ρ_t stands for the density of μ_t for all $t \geq 0$, then $(\rho_t)_t$ satisfies the following Fokker-Planck equation:

$$\frac{\partial \rho_t}{\partial t} = -\nabla \cdot (v_t \rho_t) + \lambda \Delta \rho_t, \quad (24)$$

$$v_t(x) \triangleq v(x, \mu_t) = - \int_{\mathbb{S}^{d-1}} \sum_{s \in S} p_s \psi'_{s,t,\theta}(\langle x, \theta \rangle) \theta d\theta,$$

$$\psi'_{s,t,\theta}(z) = [z - (F_{\theta_{\#}^* \nu_s}^{-1} \circ F_{\theta_{\#}^* \mu_t})(z)].$$

The proof is in the Appendix. For its proof, following that of Liutkus et al. (2019), we use the technique introduced by Jordan et al. (1998): We first prove the existence of a generalized minimizing movement scheme by showing that the solution curve $(\mu_t)_t$ is a limit of the solution of a time-discretized problem. Then we prove that the curve $(\rho_t)_t$ solves the PDE given in (24). *Interestingly, the total drift term $v(x, \mu_t)$ is essentially the total superposition of individual Kantorovich potentials from empirical distributions specified to each sensitive attribute in the sense of linearity.*

5.2. Sliced Wasserstein barycenter: connection with stochastic differential equations

The corresponding stochastic differential equation to the Fokker-Planck equation for the sliced Wasserstein barycenter of Eq. (24) is the following:

$$dX_t = v(X_t, \mu_t) dt + \sqrt{2\lambda} dW_t. \quad (25)$$

With the unbiased sampling $\bar{X}_0^i \sim \mu_0$,

$$\bar{X}_{k+1}^i = \bar{X}_k^i + h \hat{v}_k(\bar{X}_k^i) + \sqrt{2\lambda h} Z_{k+1}^i,$$

$$\hat{v}_k(x) \triangleq -(1/N_{\theta}) \sum_{n=1}^{N_{\theta}} \sum_{s \in S} p_s \psi'_{s,k,\theta_n}(\langle \theta_n, x \rangle) \theta_n,$$

$$\psi'_{s,k,\theta}(z) = [z - (F_{\theta_{\#}^* \nu_s}^{-1} \circ F_{\theta_{\#}^* \bar{\mu}_{kh}^N})(z)],$$

$$\bar{\mu}_{kh}^N = (1/N) \sum_{j=1}^N \delta_{\bar{X}_k^j}.$$

5.3. Liouville PDE-based deterministic path sampling for sliced Wasserstein barycenter

In order to reduce the variance from Monte Carlo approach, the path sampling is transformed without Monte Carlo sam-

pling based on Algorithm 1:

$$\begin{aligned}\bar{X}_{k+1}^i &= \bar{X}_k^i + h\tilde{v}_k(\bar{X}_k^i), \\ \tilde{v}_k(x) &\triangleq -(1/N_\theta) \sum_{n=1}^{N_\theta} \sum_{s \in S} p_s \psi'_{s,k,\theta_n}(\langle \theta_n, x \rangle) \theta_n \\ &\quad - \lambda \nabla \log \rho(\bar{X}_k^i, t_k), \\ \log \rho(\bar{X}_{k+1}^i, t_{k+1}) &= \log \rho(\bar{X}_k^i, t_k) - h \nabla \cdot \tilde{v}_k(\bar{X}_k^i).\end{aligned}$$

6. Main Results and Discussion

In this section, we evaluate the SWF algorithm on a synthetic real data setting. Our primary goal is to validate our theory and illustrate the behavior of our non-standard approach to obtain the state-of-the-art results in the implicit generative method. In all our experiments, the initial distribution μ_0 is selected as the standard Gaussian distribution on \mathbb{R}^d , we take $Q = 50$ quantiles and $N = 6000, 1994$, and $100,000$ samples/particles for training and testing, which proved sufficient to approximate the quantile functions accurately.

We evaluate the Liouville PDE-based SWF algorithm with the SWF from three case studies.

6.1. Case Study 1: Optimal transport of probability distribution from source to target

We perform the first set of experiments on synthetic data where we consider a standard Gaussian mixture model (GMM) with 10 components and random parameters. Centroids are taken as sufficiently distant from each other to make the problem more challenging. We generate $P = 50000$ data samples in each experiment. In our first experiment, we set $d = 2$ for visualization purposes and illustrate the general behavior of the algorithm. Figure 1 shows the evolution of the particles through the iteration. Here, we set $N_\theta = 30$, $h = 1$ and $\lambda = 10^{-4}$. We first observe that the SW cost between the empirical distributions of training data and particles is steadily decreasing along the SW flow. Furthermore, we see that the quantile functions (QFs), $F_{\theta_\mu^* \mu_{k,h}^N}$ that are computed with the initial set of particles (the training stage) can be perfectly re-used for new unseen particles in a subsequent test stage, yielding similar – yet slightly higher – SW cost. The performances between Liouville PDE-based SWF and the vanilla SWF are compared in Figure 1 and Table 1. The utilized loss function is Eq. (11).

6.2. Case Study 2: Sliced Wasserstein flow for barycenter

The setting is similar to Case Study 1, and the barycenter from two GMM distributions is computed from the vanilla SWF and the Liouville PDE-based SWF (Figure 2). The

utilized loss function is Eq. (23).

6.3. Case Study 3: Fair regression with sliced Wasserstein barycenter

For the cases of communities and crime and health care spending cost, the KS score from the Liouville PDE-based SWF barycenter is better than the exact Wasserstein barycenter. Also, Liouville PDE-based SWF barycenter does improve the accuracy (MSE) and/or fairness (KS) in the mean values and/or variances. When the data is in high-dimensional spaces and the computation of the exact Wasserstein barycenter is not tractable, sliced barycenters can provide an alternative approximation.

Communities and Crime (CRIME) The CRIME dataset contains socio-economic, law enforcement, and crime data about communities in the US (Redmond & Baveja, 2022) with 1994 examples. The task is to predict the number of violent crimes per 10^5 population (normalized to $[0,1]$) with race as the protected attribute. Following Calders et al. (2013), Chzhen et al. 2020 made a binary sensitive attribute s as to the percentage of the black population, which yielded 970 instances of $s = 1$ with a mean crime rate 0.35 and 1024 instances of $s = -1$ with a mean crime rate 0.13. For each community (sample), the sensitive attribute PctRace is categorized among Black, White, and Asian populations with the maximum racial proportion.

Health care spending Zink & Rose (2019) selected a random sample of 100,000 enrollees from the IBM MarketScan Research Databases. Diagnosed health conditions took the form of the established Hierarchical Condition Category (HCC) variables created for risk adjustment. We considered the 79 HCC variables currently used in Medicare Advantage risk adjustment formulas and retained the 62 HCCs that had at least 30 enrollees with the condition. The sensitive attributes are age of participants (AGE), binary indicator for female (sexF), and total payments (totpay).

6.4. Pareto curves of accuracy (Mean Squared Error) versus fairness (Kolmogorov-Smirnov Score)

The Pareto curves (Figure 3) demonstrate exact Wasserstein barycenters attain low MSE but incur large KS disparities. Both SWF-based methods substantially reduce fairness violations, with the Liouville PDE-based SWF consistently achieving more favorable Pareto trade-offs, yielding lower KS at comparable or lower MSE across datasets and sensitive attributes. We evaluate how imposing the Liouville PDE constraint alters the fairness–accuracy tradeoff in the sliced Wasserstein Flow.

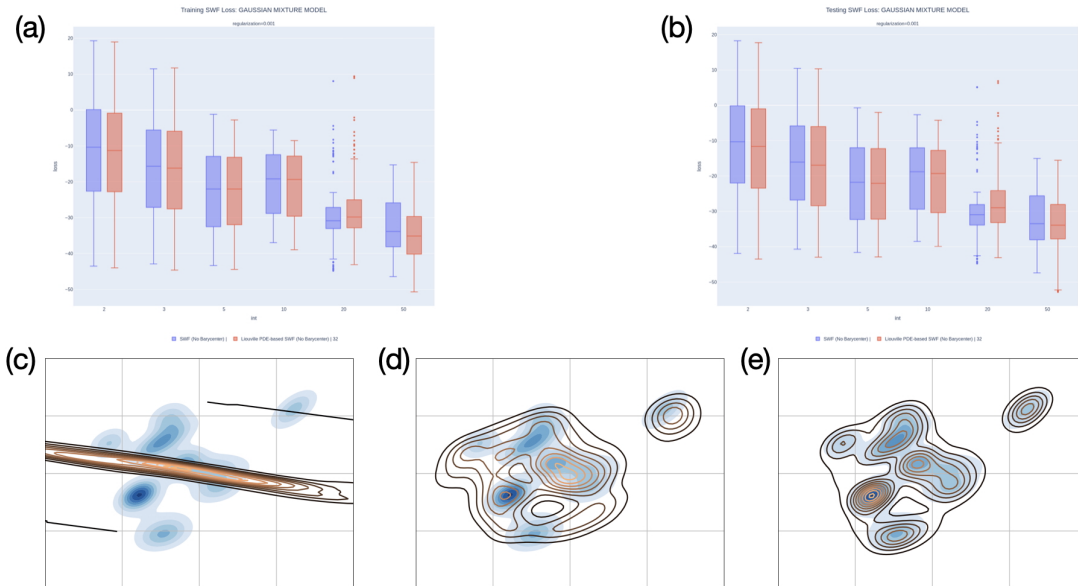


Figure 1. Sliced Wasserstein flows (SWF) (a) and (b) Training and testing the optimal transport to the defined target distribution. Two approaches are compared: the vanilla SWF (Liutkus et al., 2019) and the proposed Liouville PDE-based SWF. (c)-(e) The target distribution (shaded contour plot) and the initial, intermediate, and distribution of particles (isopotential lines) in the converging Liouville PDE-based SWF.

COMMUNITIES AND CRIMES

Based on Figure S1, across regularization levels, mild regularization ($\lambda \leq 0.01$) yields simultaneous reductions in KS with only marginal changes in MSE, indicating an improved accuracy–fairness trade-off relative to the unregularized case. The Liouville PDE-based SWF consistently attains lower or comparable KS than the vanilla SWF, reflecting enhanced stability on fairness under sensitive-attribute conditioning on *PctRace*. As λ increases further, both methods exhibit degraded performance, with sharp increases in MSE and no corresponding fairness gains, consistent with over-regularization. Overall, these results confirm that PDE-based regularization provides meaningful fairness improvements at low-to-moderate λ without sacrificing predictive accuracy.

HEALTH CARE SPENDING COST

Based on Figures S2 - S4. Across all sensitive attributes, low-to-moderate regularization ($\lambda \leq 0.1$) preserves predictive accuracy while yielding comparable or reduced KS values relative to the unregularized case, indicating a stable accuracy–fairness trade-off. The Liouville PDE-based SWF generally exhibits equal or lower KS than the vanilla SWF, particularly for *AGE* and *totpay*, suggesting improved control of distributional disparities under sensitive-attribute conditioning. In contrast, strong regularization ($\lambda = 1$) leads to pronounced degradation in MSE for both methods without consistent fairness gains, reflecting over-regularization.

Overall, these results demonstrate that PDE-based regularization provides robust fairness improvements across heterogeneous health-related sensitive attributes while maintaining accuracy in the practically relevant low- λ regime.

6.5. Computational usage

We additionally assess the computational overhead introduced by the Liouville PDE. To isolate the implementation effects, we compare the wall-clock execution time and peak memory usage between the vanilla SWF and its Liouville PDE under variations in ODE layer size and regularization. Across both datasets, the PDE constraint produces only marginal increases in runtime and memory consumption, indicating that the fairness and accuracy improvements reported earlier are obtained at negligible computational cost.

Across variations in neural ODE layer width and regularization strength, both the Liouville PDE-based SWF and the vanilla SWF exhibit stable and nearly invariant computational cost. For the Communities and Crime dataset, execution time varies within a narrow range (approximately 17.1 - 18.2 s), while peak memory usage remains tightly bounded (about 2477 - 2498 MB) (Table S5, S7). Similarly, for the Health Care Spending Cost dataset, execution times fluctuate modestly with architecture and regularization (approximately 174 - 180 s), and peak memory usage remains confined to a narrow band (about 3358 - 3369 MB) (Table S6, S8). The vanilla SWF baseline, which does not employ

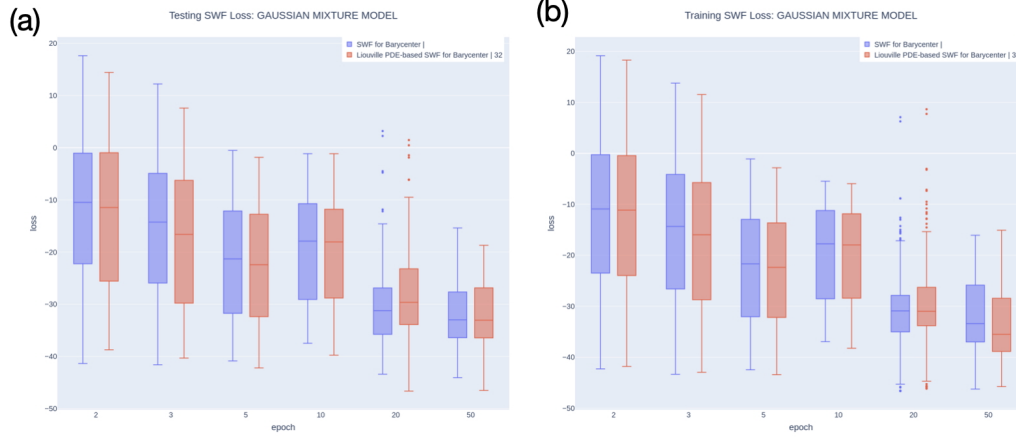


Figure 2. Sliced Wasserstein barycenter flows (SWF barycenter versus Liouville PDE-based SWF barycenter) with 2 Gaussian Mixture Models (GMM).

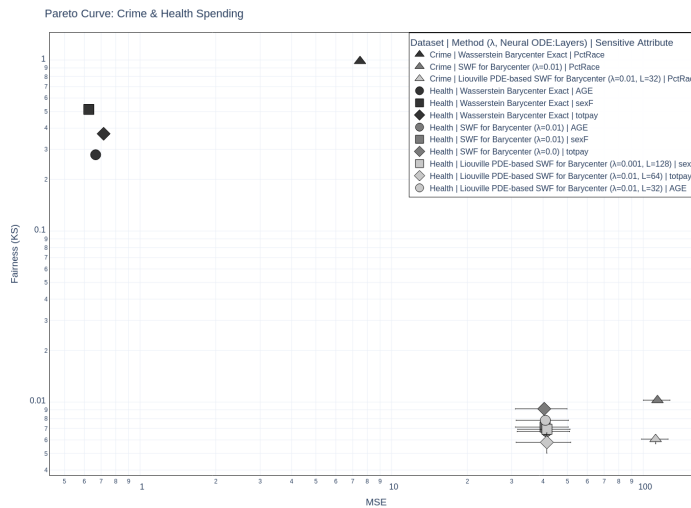


Figure 3. Pareto curves showing the accuracy (MSE)–fairness (KS) tradeoff for crime and health spending datasets. Each point corresponds to a model paired with a sensitive attribute.

a neural ODE, exhibits comparable runtime and memory profiles. These small variations indicate that the observed improvements in fairness (KS) and accuracy (MSE) are not attributable to increased computational load, but instead reflect genuine modeling differences introduced by the Liouville PDE-based formulation.

7. Conclusion

The Liouville PDE-based sliced-Wasserstein flows provide improved convergence with reduced loss and/or reduced variance. In the high-dimensionality of around 60 and 120, the accuracy and/or fairness are improved from Liouville-PDE based SWF barycenter in comparison to the SWF, and also as a reasonable alternative in comparison to the exact Wasserstein barycenter, where computational

complexity exceedingly elevates.

When the exact Wasserstein barycenter is computationally heavy, the approximate sliced-Wasserstein barycenter from Liouville PDE is useful broadly in high-dimensional statistics. The Pareto curves of accuracy and fairness in high-dimension with sensitive attributes from Liouville PDE will provide diverse aspects of decision making with rationalized fairness. In characterizing the Pareto curves in high dimensional distributions, two showcases of community crimes and health care spending costs are considered. The competence of Liouville PDE-based improvement in convergence and reduction in variance needs more exploration from diverse datasets. Moreover, the theoretical analysis of stability and convergence of the Liouville PDE-based SWF remains for the future.

Acknowledgements

JC and PL were partially supported by NIH Data Science and NIMHD grant, 3U54MD013376-04S3. PL is partially supported by Center for Equitable AI and Machine Learning Systems (CEAMLS) Affiliated Project (ID: 10072401).

Impact Statement

This paper presents work whose goal is to advance the field of Machine Learning. There are many potential societal consequences of our work, none which we feel must be specifically highlighted here.

References

- Agarwal, A., Beygelzimer, A., Dudik, M., Langford, J., and Wallach, H. A reductions approach to fair classification. In *Proceedings of the 35th International Conference on Machine Learning*, 2018.
- Agarwal, A., Dudik, M., and Wu, Z. Fair regression: quantitative definitions and reduction-based algorithms. In *Proceedings of the 36th International Conference on Machine Learning*, 2019.
- Agueh, M. and Carlier, G. Barycenters in the Wasserstein space. *SIAM Journal on Mathematical Analysis*, 43:904–924, 2011.
- Albergo, M. and Vanden-Eijnden, E. Building normalizing flows with stochastic interpolants. In *International Conference on Learning Representations*, 2023.
- Ambrosio, L., Gigli, N., and Savare, G. *Gradient flows in metric spaces and in the space of probability measures*. Birkhauser, second edition edition, 2008.
- Berk, R., Heidari, H., Jabbari, S., Joseph, M., Kearns, M., Morgenstern, J., Neel, S., and Roth, A. A convex framework for fair regression. *arXiv*, pp. 1706.02409, 2017.
- Boffi, N. and Vanden-Eijnden, E. Probability flow solution of the Fokker-Planck equation. *Machine Learning: Science and Technology*, 4:035012, 2023.
- Bonneel, N., Rabin, J., Peyre, G., and Pfister, H. Sliced and radon wasserstein barycenters of measures. *J. Math Imaging Vis.*, 51:22–45, 2015.
- Bonnotte, N. *Unidimensional and evolution methods for optimal transportation*. PhD thesis, Universite Paris Sud - Parix XI; Scuola normale superiore, 2013.
- Brenier, Y. and Benamou, J.-D. A computational fluid mechanics solution to the Monge-Kantorovich mass transfer problem. *Numerische Mathematik*, 84:375–393, 2000.
- Brockett, R. Notes on the control of the Liouville equation. *Control of partial differential equations, Lecture Note in Mathematics*, pp. 101–129, 2012.
- Calders, T., Karim, A., Kamiran, F., Ali, W., and Zhang, X. Controlling attribute effect in linear regression. In *IEEE International Conference on Data Mining*, 2013.
- Chen, R., Rubanova, Y., Bettencourt, J., and Duvenaud, D. Neural ordinary differential equations. *NeurIPS*, 2018.
- Chen, Y., Georgiou, T., and Pavon, M. Stochastic control liaisons: Richard Sinkhorn meets Gaspard Monge on a Schrodinger bridge. *SIAM Review*, 63, 2021.
- Cheng, X., Lu, J., Tan, Y., and Xie, Y. Convergence of flow-based generative models via proximal gradient descent in Wasserstein space. *IEEE Transactions on Information Theory*, 70:8087–8106, 2024.
- Chiappa, S., Jiang, R., Stepleton, T., Pacchiano, A., Jiang, H., and Aslanides, J. A general approach to fairness with optimal transport. In *The Thirty-Fourth AAAI Conference on Artificial Intelligence*, 2020.
- Chzhen, E. and Schreuder, N. A minimax framework for quantifying risk-fairness trade-off in regression. *The Annals of Statistics*, 50:2416–2442, 2022.
- Chzhen, E., Denis, C., Hebiri, M., and Oneto, L. Fair regression with Wasserstein barycenters. *34th Conference on Neural Information Processing Systems*, 2020.
- Cuturi, M. and Doucet, A. Fast computation of Wasserstein barycenters. In *The 31st International Conference on Machine Learning*, volume 32, 2014.
- Deshpande, I., Zhang, Z., and Schwing, A. Generative modeling using the sliced Wasserstein distance. In *Proceedings of the IEEE Conference on Computer Vision and Pattern Recognition*, pp. 3483–3491, 2018.
- Grathwohl, W., Chen, R., Bettencourt, J., Sutskever, I., and Duvenaud, D. Ffjord: Free-form continuous dynamics for scalable reversible generative models. In *International Conference on Learning Representations*, 2019.
- Jiang, R., Pacchiano, A., Stepleton, T., Jiang, H., and Chiappa, S. Wasserstein fair classification. In *Proceedings of The 35th Uncertainty in Artificial Intelligence Conference*, volume 115, pp. 862–872, 2019.
- Jordan, R., Kinderlehrer, D., and Otto, F. The variational formulation of the Fokker-Planck equation. *SIAM Journal on Mathematical Analysis*, 29:1–17, 1998.
- Kolesov, A., Mokrov, P., Udovichenko, I., Gazdieva, M., Pammer, G., Burnaev, E., and Korotin, A. Estimating barycenters of distributions with neural optimal transport.

- In *Proceedings of the 41st International Conference on Machine Learning*, volume 235, 2024.
- Kolouri, S., Zou, Y., and Rohde, G. Sliced Wasserstein kernels for probability distributions. In *Proceedings of the IEEE Conference on Computer Vision and Pattern Recognition (CVPR)*, pp. 5258–5267, 2016.
- Kroshnin, A., Dvinskikh, D., Dvurechensky, P., Gasnikov, A., tupitsa, N., and Uribe, C. On the complexity of approximating Wasserstein barycenters. In *Proceedings of the 36th International Conference on Machine Learning*, 2019.
- Lin, T., Ho, N., Chen, X., Cuturi, M., and Jordan, M. Fixed-support Wasserstein barycenters: computational hardness and fast algorithm. *34th Conference on Neural Information Processing Systems*, 2020.
- Liutkus, A., Simsekli, U., Majewski, S., Durmus, A., and Stoter, F.-R. Sliced-Wasserstein flows: nonparametric generative modeling via optimal transport and diffusions. In *Proceedings of the 36th International Conference on Machine Learning*, 2019.
- Nadjahi, K., Durmus, A., Chizat, L., Kolouri, S., Shahrampour, S., and Simsekli, U. Statistical and topological properties of sliced probability divergences. *34th Conference on Neural Information Processing Systems*, 2020.
- Nelson, E. *Dynamical Theories of Brownian Motion*. Princeton University, 1967.
- Rabin, J., Peyre, G., Delon, J., and Bernot, M. Wasserstein barycenter and its application to texture mixing. In *International Conference on Scale Space and Variational Methods in Computer Vision*, pp. 435–446, 2011.
- Redmond, M. and Baveja, A. A data-driven software tool for enabling cooperative information sharing among police departments. *European Journal of Operational Research*, 141:660–678, 2022.
- Shen, Z., Wang, Z., Kale, S., Ribeiro, A., Karbasi, A., and Hassani, H. Self-consistency of the Fokker-Planck equation. In Loh, P.-L. and Raginsky, M. (eds.), *Proceedings of Machine Learning Research*, volume 178, pp. 1–25, 2022.
- Steinberg, D., Reid, A., and O’Callaghan, S. Fairness measures for regression via probabilistic classification. In *2nd Ethics of Data Science Conference (EDSC 2020)*, Sydney, Australia, 2020.
- T. Le Gouic, J.-M. Loubes, P. R. Projection to fairness in statistical learning. *arXiv*, pp. 2005.11720, 2020.
- Tabak, E. and Turner, C. A family of nonparametric density estimation algorithms. *Communications on Pure and Applied Mathematics*, 46:0145–0164, 2013.
- Wang, F., Cheng, L., Guo, R., Liu, K., and Yu, P. Equal opportunity of coverage in fair regression. In *37th Conference on Neural Information Processing Systems*, 2023.
- Xu, C., Cheng, X., and Xie, Y. Normalizing flow neural networks by jko scheme. In *37th Conference on Neural Information Processing Systems*, 2023.
- Zink, A. and Rose, S. Fair regression for health care spending. *Biometrics*, 76(973-982), 2019.

A. Proof of Theorem 3

The proof is an extension for sliced-Wasserstein barycenter based on Liutkus, et al. (Liutkus et al., 2019). We first need to generalize Bonnotte, et al. (Bonnotte, 2013) [Lemma 5.4.3] to distribution $\rho \in L^\infty(\bar{B}(0, r))$, $r > 0$.

Theorem S1. *Let ν be a probability measure on $\bar{B}(0, 1)$ with a strictly positive smooth density. Fix a time step $h > 0$, regularization constant $\lambda > 0$ and a radius $r > \sqrt{d}$. For any probability measure μ_0 on $\bar{B}(0, r)$ with density $\rho_0 \in L^\infty(\bar{B}(0, r))$, there is a probability measure μ on $\bar{B}(0, r)$ minimizing:*

$$\mathcal{G}(\mu) = \mathcal{F}_\lambda^{\{\nu_s\}}(\mu) + \frac{1}{2h} \mathcal{W}_2^2(\mu, \mu_0),$$

where $\mathcal{F}_\lambda^{\{\nu_s\}}$ is given by (23). Moreover the optimal μ has a density ρ on $\bar{B}(0, r)$ and:

$$|\rho|_{L^\infty} \leq (1 + h/\sqrt{d})^d |\rho_0|_{L^\infty}. \quad (\text{S1})$$

Proof. The set of measures supported on $\bar{B}(0, r)$ is compact in the topology given by \mathcal{W}_2 metric. Furthermore by Ambrosio et al (Ambrosio et al., 2008) [Lemma 9.4.3] \mathcal{H} is lower semicontinuous on $(\mathcal{P}(\bar{B}(0, r)), \mathcal{W}_2)$. Since by (Bonnotte, 2013)[Proposition 5.1.2, Proposition 5.1.3], \mathcal{SW}_2 is a distance on $\mathcal{P}(\bar{B}(0, r))$, dominated by $d^{-1/2}\mathcal{W}_2$, we have:

$$|\mathcal{SW}_2(\pi_0, \nu) - \mathcal{SW}_2(\pi_1, \nu)| \leq \mathcal{SW}_2(\pi_0, \pi_1) \leq \frac{1}{\sqrt{d}} \mathcal{W}_2(\pi_0, \pi_1).$$

The above means that $\mathcal{SW}_2(\cdot, \nu)$ is continuous with respect to topology given by \mathcal{W}_2 , which implies that $\mathcal{SW}_2^2(\cdot, \nu)$ is continuous in this topology as well. Therefore $\mathcal{G} : \mathcal{P}(\bar{B}(0, r)) \rightarrow (-\infty, +\infty]$ is a lower semicontinuous function on the compact set $(\mathcal{P}(\bar{B}(0, r)), \mathcal{W}_2)$. Hence there exists a minimum ν of \mathcal{G} on $\mathcal{P}(\bar{B}(0, r))$. Furthermore, since $\mathcal{H}(\pi) = +\infty$ for measures π that do not admit a density with respect to Lebesgue measure, the measure μ must admit a density ρ .

If ρ_0 is smooth and positive on $\bar{B}(0, r)$, the inequality S1 is true by (Bonnotte, 2013)[Lemma 5.4.3.] When ρ_0 is just in $L^\infty(\bar{B}(0, r))$, we proceed by smoothing. For $t \in (0, 1]$, let ρ_t be a function obtained by convolution of ρ_0 with a Gaussian kernel $(t, x, y) \mapsto (2\pi)^{d/2} \exp(-|x - y|^2/2)$, restricting the result to $\bar{B}(0, r)$ and normalizing to obtain a probability density. Then $(\rho_t)_t$ are smooth positive densities, and it is easy to see that $\lim_{t \rightarrow 0} |\rho_t|_{L^\infty} \leq |\rho_0|_{L^\infty}$. Furthermore, if we denote by μ_t the measure on $\bar{B}(0, r)$ with density ρ_t , then μ_t converge weakly to μ_0 . For $t \in (0, 1]$ let $\hat{\mu}_t$ be the minimum of $\mathcal{F}_\lambda^{\{\nu_s\}}(\cdot) + \frac{1}{2h} \mathcal{W}_2^2(\cdot, \mu_t)$, and let $\hat{\rho}_t$ be the density of $\hat{\mu}_t$. Using Bonnotte, et al. (Bonnotte, 2013)[Lemma 5.4.3.] we get

$$|\hat{\rho}_t|_{L^\infty} \leq (1 + h\sqrt{d})^d |\rho_t|_{L^\infty},$$

so $\hat{\rho}_t$ lies in a ball of finite radius in L^∞ . Using compactness of $\mathcal{P}(\bar{B}(0, r))$ in weak topology and compactness of closed ball in $L^\infty(\bar{B}(0, r))$ in weak star topology, we can choose a subsequence $\hat{\mu}_{t_k}, \hat{\rho}_{t_k}, \lim_{k \rightarrow +\infty} t_k = 0$, that converges along that subsequence to limits $\hat{\mu}, \hat{\rho}$. Obviously $\hat{\rho}$ is the density of $\hat{\mu}$, since for any continuous function f on $\bar{B}(0, r)$ we have:

$$\int \hat{\rho} f dx = \lim_{k \rightarrow \infty} \int \rho_{t_k} f dx = \lim_{k \rightarrow \infty} \int f d\mu_{t_k} = \int f d\mu.$$

Furthermore, since $\hat{\rho}$ is the weak star limit of a bounded subsequence, we have:

$$|\hat{\rho}|_{L^\infty} \leq \limsup_{k \rightarrow \infty} (1 + h\sqrt{d})^d |\rho_{t_k}|_{L^\infty} \leq (1 + h\sqrt{d})^d |\rho_0|_{L^\infty}.$$

To finish, we just need to prove that $\hat{\mu}$ is a minimum of \mathcal{G} . We remind our reader, that we already established existence of some minimum μ (that might be different from $\hat{\mu}$). Since $\hat{\mu}_{t_k}$ converges weakly to $\hat{\mu}$ in $\mathcal{P}(\bar{B}(0, r))$, it implies convergence in \mathcal{W}_2 as well since $\bar{B}(0, r)$ is compact. Similarly μ_{t_k} converges to μ_0 in \mathcal{W}_2 . Using the lower semicontinuity of \mathcal{G} we now have:

$$\begin{aligned} \mathcal{F}_\lambda^{\{\nu_s\}}(\hat{\mu}) + \frac{1}{2h} \mathcal{W}_2^2(\hat{\mu}, \mu_0) &\leq \liminf_{k \rightarrow \infty} (\mathcal{F}_\lambda^{\{\nu_s\}}(\hat{\mu}_{t_k}) + \frac{1}{2h} \mathcal{W}_2^2(\hat{\mu}_{t_k}, \mu_0)) \\ &\leq \liminf_{k \rightarrow \infty} \mathcal{F}_\lambda^{\{\nu_s\}}(\mu) + \frac{1}{2h} \mathcal{W}_2^2(\mu, \mu_{t_k}) + \frac{1}{2h} \mathcal{W}_2^2(\hat{\mu}_{t_k}, \mu_0) - \frac{1}{2h} \mathcal{W}_2^2(\hat{\mu}_{t_k}, \mu_{t_k}) \\ &= \mathcal{F}_\lambda^{\{\nu_s\}}(\mu) + \frac{1}{2h} \mathcal{W}_2^2(\mu, \mu_0), \end{aligned}$$

where the second inequality comes from the fact, that $\hat{\mu}_{t_k}$ minimizes $\mathcal{F}_\lambda^{\{\nu_s\}} + \frac{1}{2h} \mathcal{W}_2^2(\cdot, \mu_{t_k})$. From the above inequality and previously established facts, it follows that $\hat{\mu}$ is a minimum of \mathcal{G} with density satisfying S1. \square

Definition S1 (Minimizing movement scheme, (Liutkus et al., 2019)). Let $r > 0$ and $\mathcal{F} : \mathbb{R}_+ \times \mathcal{P}(\bar{B}(0, r)) \times \mathcal{P}(\bar{B}(0, r)) \rightarrow \mathbb{R}$ be a functional. Let $\mu_0 \in \mathcal{P}(\bar{B}(0, r))$ be a starting point. For $h > 0$ a piecewise constant trajectory $\mu_h : [0, \infty) \rightarrow \mathcal{P}(\bar{B}(0, r))$ for \mathcal{F} starting at μ_0 is a function such that:

- $\mu^h(0) = \mu_0$.
- μ^h is constant on each interval $[nh, (n+1)h)$, so $\mu^h(t) = \mu^h(nh)$ with $n = \lfloor t/h \rfloor$.
- $\mu^h((n+1)h)$ minimizes the function $\zeta \mapsto \mathcal{F}(h, \zeta, \mu^h(nh))$, for all $n \in \mathbb{N}$.

We say $\hat{\mu}$ is a minimizing movement scheme for \mathcal{F} starting at μ_0 , if there exists a family of piecewise constant trajectory $(\mu^h)_{h>0}$ for \mathcal{F} such that $\hat{\mu}$ is a pointwise limit of μ^h as h goes to 0, i.e. for all $t \in \mathbb{R}_+$, $\lim_{h \rightarrow 0} \mu^h(t) = \mu(t)$ in $\mathcal{P}(\bar{B}(0, r))$. We say that $\tilde{\mu}$ is a generalized minimizing movement for \mathcal{F} starting at μ_0 , if there exists a family of piecewise constant trajectory $(\mu^h)_{h>0}$ for \mathcal{F} and a sequence $(h_n)_n$, $\lim_{n \rightarrow \infty} h_n = 0$, such that μ^{h_n} converges pointwise to $\tilde{\mu}$.

Theorem S2. Let ν be a probability measure on $\bar{B}(0, 1)$ with a strictly positive smooth density. Fix a regularization constant $\lambda > 0$ and radius $r > \sqrt{d}$. Given an absolutely continuous measure $\mu_0 \in \mathcal{P}(\bar{B}(0, r))$ with density $\rho_0 \in L^\infty(\bar{B}(0, r))$, there is a generalized minimizing movement scheme $(\mu_t)_t$ in $\mathcal{P}(\bar{B}(0, r))$ starting from μ_0 for the functional defined by

$$\mathcal{F}^{\{\nu_s\}}(h, \mu_+, \mu_-) = \mathcal{F}_\lambda^{\{\nu_s\}}(\mu_+) + \frac{1}{2h} \mathcal{W}_2^2(\mu_+, \mu_-). \quad (\text{S2})$$

Moreover for any time $t > 0$, the probability measure $\mu_t = \mu(t)$ has density ρ_t with respect to the Lebesgue measure and:

$$|\rho_t|_{L^\infty} \leq e^{dt\sqrt{d}} |\rho_0|_{L^\infty}. \quad (\text{S3})$$

Proof. We start by noting, that by S1 for any $h > 0$ there exists a piecewise constant trajectory μ^h for S2 starting at μ_0 . Furthermore for $t \geq 0$ measure $\mu_t^h = \mu^h(t)$ has density ρ_t^h , and:

$$|\rho_t^h|_{L^\infty} \leq e^{d\sqrt{d}(t+h)} |\rho_0|_{L^\infty}. \quad (\text{S4})$$

Let us choose $T > 0$. We denote $\rho^h(t, x) = \rho_t^h(x)$. For $h \leq 1$, the functions ρ^h lie in a ball in $L^\infty([0, T] \times \bar{B}(0, r))$, so from Banach-Alaoglu theorem there is a sequence h_n converging to 0, such that ρ^{h_n} converges in weak-star topology in $L^\infty([0, T] \times \bar{B}(0, r))$ to a certain limit ρ . Since ρ has to be nonnegative except for a set of measure zero, we assume ρ is nonnegative. We denote $\rho_t(x) = \rho(t, x)$. We will prove that for almost all t , ρ_t is a probability density and $\mu_t^{h_n}$ converges in \mathcal{W}_2 to a measure μ_t with density ρ_t .

First of all, for almost all $t \in [0, T]$, ρ_t is a probability density, since for any Borel set $A \subseteq [0, T]$ the indicator of set $A \times \bar{B}(0, r)$ is integrable, and hence by definition of the weak-star topology:

$$\int_A \int_{\bar{B}(0, r)} \rho_t(x) dx dt = \lim_{n \rightarrow \infty} \int_A \int_{\bar{B}(0, r)} \rho_t^{h_n}(x) dx dt,$$

and so we have to have $\int \rho_t(x) dx = 1$ for almost all $t \in [0, T]$. Nonnegativity of ρ_t follows from nonnegativity of ρ .

We will now prove, that for almost all $t \in [0, T]$ the measures $\mu_t^{h_n}$ converge to a measure with density ρ_t . Let $t \in (0, T)$, take $\delta < \min(T - t, t)$ and $\zeta \in C^1(\bar{B}(0, r))$. We have:

$$\begin{aligned} & \left| \int_{\bar{B}(0, r)} \zeta d\mu_t^{h_n} - \int_{\bar{B}(0, r)} \zeta d\mu_t^{h_m} \right| \leq \\ & \left| \int_{\bar{B}(0, r)} \zeta d\mu_t^{h_n} - \frac{1}{2\delta} \int_{t-\delta}^{t+\delta} \int_{\bar{B}(0, r)} \zeta d\mu_s^{h_n} ds \right| + \left| \int_{\bar{B}(0, r)} \zeta d\mu_t^{h_m} - \frac{1}{2\delta} \int_{t-\delta}^{t+\delta} \int_{\bar{B}(0, r)} \zeta d\mu_s^{h_m} ds \right| + \\ & \left| \frac{1}{2\delta} \int_{t-\delta}^{t+\delta} \int_{\bar{B}(0, r)} \zeta d\mu_s^{h_m} ds - \frac{1}{2\delta} \int_{t-\delta}^{t+\delta} \int_{\bar{B}(0, r)} \zeta d\mu_s^{h_n} ds \right|. \end{aligned} \quad (\text{S5})$$

Because $\mu_t^{h_n}$ have densities $\rho_t^{h_n}$ and both ρ^{h_n}, ρ^{h_m} converge to ρ in weak-star topology, the last element of the sum on the right hand side converges to zero, as $n, m \rightarrow \infty$. Next, we get a bound on the other two terms.

First, if we denote by γ the optimal transport plan between $\mu_t^{h_n}$ and $\mu_s^{h_n}$, we have:

$$\left| \int_{\bar{B}(0,r)} \zeta d\mu_t^{h_n} - \int_{\bar{B}(0,r)} \zeta d\mu_s^{h_n} \right|^2 \leq \int_{\bar{B}(0,r) \times \bar{B}(0,r)} |\zeta(x) - \zeta(y)|^2 d\gamma(x,y) \leq |\nabla \zeta|_\infty^2 \mathcal{W}_2^2(\mu_t^{h_n}, \mu_s^{h_n}). \quad (\text{S6})$$

In addition, for $n_t = \lfloor t/h_n \rfloor$ and $n_s = \lfloor s/h_n \rfloor$ we have $\mu_t^{h_n} = \mu_{n_t h_n}^{h_n}$ and $\mu_s^{h_n} = \mu_{n_s h_n}^{h_n}$. For all $k \geq 0$ we have:

$$\mathcal{W}_2^2(\mu_{k h_n}^{h_n}, \mu_{(k+1) h_n}^{h_n}) \leq 2h_n (\mathcal{F}_\lambda^{\{\nu_s\}}(\mu_{k h_n}^{h_n}) - \mathcal{F}_\lambda^{\{\nu_s\}}(\mu_{(k+1) h_n}^{h_n})). \quad (\text{S7})$$

Using this result and (S6) and assuming without loss of generality $n_t \leq n_s$, from the Cauchy-Schwartz inequality we get:

$$\begin{aligned} \mathcal{W}_2^2(\mu_t^{h_n}, \mu_s^{h_n}) &\leq \left(\sum_{k=n_t}^{n_s-1} \mathcal{W}_2(\mu_{k h_n}^{h_n}, \mu_{(k+1) h_n}^{h_n}) \right)^2 \\ &\leq |n_t - n_s| \sum_{k=n_t}^{n_s-1} \mathcal{W}_2^2(\mu_{k h_n}^{h_n}, \mu_{(k+1) h_n}^{h_n}) \\ &\leq 2h_n |n_t - n_s| (\mathcal{F}_\lambda^{\{\nu_s\}}(\mu_{n_t h_n}^{h_n}) - \mathcal{F}_\lambda^{\{\nu_s\}}(\mu_{n_s h_n}^{h_n})) \leq 2C(|t - s| + h_n), \end{aligned} \quad (\text{S8})$$

where we used for the last inequality, denoting $C = \mathcal{F}_\lambda^{\{\nu_s\}}(\mu_0) - \min_{\mathcal{P}(\bar{B}(0,r))} \mathcal{F}_\lambda^{\{\nu_s\}}$, that $(\mathcal{F}_\lambda^{\{\nu_s\}}(\mu_{k h_n}^{h_n}))_n$ is non-increasing by (S7) and $\min_{\mathcal{P}(\bar{B}(0,r))} \mathcal{F}_\lambda^{\{\nu_s\}}$ is finite since $\mathcal{F}_\lambda^{\{\nu_s\}}$ is lower semi-continuous. Finally, using Jensen's inequality, the above bound and (S6) we get:

$$\begin{aligned} \left| \int_{\bar{B}(0,r)} \zeta d\mu_t^{h_n} - \frac{1}{2\delta} \int_{t-\delta}^{t+\delta} \int_{\bar{B}(0,r)} \zeta d\mu_s^{h_n} ds \right|^2 &\leq \frac{1}{2\delta} \int_{t-\delta}^{t+\delta} \left| \int_{\bar{B}(0,r)} \zeta d\mu_t^{h_n} - \int_{\bar{B}(0,r)} \zeta d\mu_s^{h_n} \right|^2 ds \\ &\leq \frac{C|\nabla \zeta|_\infty^2}{\delta} \int_{t-\delta}^{t+\delta} (|t - s| + h_n) ds \\ &\leq 2C|\nabla \zeta|_\infty^2 (h_n + \delta). \end{aligned}$$

Together with (S5), when taking $\delta = h_n$, this result means that $\int_{\bar{B}(0,r)} \zeta d\mu_t^{h_n}$ is a Cauchy sequence for all $t \in (0, T)$. On the other hand, since ρ^{h_n} converges to ρ in weak-star topology on L^∞ , the limit of $\int_{\bar{B}(0,r)} \zeta d\mu_t^{h_n}$ has to be $\int_{\bar{B}(0,r)} \zeta(x) \rho_t(x) dx$ for almost all $t \in (0, T)$. This means that for almost all $t \in [0, T]$ sequence $\mu_t^{h_n}$ converges to a measure μ_t with density ρ_t . Let $S \in [0, T]$ be the set of times such that for $t \in S$ sequence $\mu_t^{h_n}$ converges to a measure μ_t . As we established almost all points from $[0, T]$ belong to S . Let $t \in [0, T] \setminus S$. Then, there exists a sequence of times $t_k \in S$ converging to t , such that μ_{t_k} converge to some limit μ_t . We have:

$$\mathcal{W}_2(\mu_t^{h_n}, \mu_t) \leq \mathcal{W}_2(\mu_t^{h_n}, \mu_{t_k}^{h_n}) + \mathcal{W}_2(\mu_{t_k}^{h_n}, \mu_{t_k}) + \mathcal{W}_2(\mu_{t_k}, \mu_t).$$

From which we have for all $k \geq 1$:

$$\limsup_{n \rightarrow \infty} \mathcal{W}_2(\mu_t^{h_n}, \mu_t) \leq \mathcal{W}_2(\mu_{t_k}, \mu_t) + \limsup_{n \rightarrow \infty} \mathcal{W}_2(\mu_t^{h_n}, \mu_{t_k}^{h_n}),$$

and using (S8), we get $\mu_t^{h_n} \rightarrow \mu_t$. Furthermore, the measure μ_t has to have density, since $\rho_t^{h_n}$ lies in a ball in $L^\infty(\bar{B}(0, r))$, so we can choose a subsequence of $\rho_t^{h_n}$ converging in weak-star topology to a certain limit $\hat{\rho}_t$, which is the density of μ_t . We use now the diagonal argument to get convergence for all $t > 0$. Let $(T_k)_{k=1}^\infty$ be a sequence of times increasing to infinity. Let h_n^1 be a sequence converging to 0, such that $\mu_t^{h_n^1}$ converge to μ_t for all $t \in [0, T_1]$. Using the same arguments as above, we can choose a subsequence h_n^2 of h_n^1 , such that $\mu_t^{h_n^2}$ converges to a limit μ_t for all $t \in [0, T_2]$. Inductively, we construct subsequences h_n^k , and in the end take $h_n = h_n^n$. For this subsequence we have that $\mu_t^{h_n}$ converges to μ_t for all $t > 0$, and μ_t has a density satisfying the bound from the statement of the theorem.

Finally, note that (S2) follows from (S4). \square

Theorem S3. *Let $(\mu_t)_{t \geq 0}$ be a generalized minimizing movement scheme given by Theorem S3 with initial distribution μ_0 with density $\rho_0 \in L(\bar{B}(0, r))$. We denote by ρ_t the density of μ_t for all $t \geq 0$. Then ρ_t satisfies the continuity equation:*

$$\frac{\partial \rho_t}{\partial t} + \nabla \cdot (v_t \rho_t) + \lambda \Delta \rho_t = 0, \quad v_t(x) = - \int_{\mathbb{S}^{d-1}} \sum_s p_s \psi'_{s,t,\theta}(\langle x, \theta \rangle) \theta d\theta,$$

in a weak sense, that is for all $\xi \in C_c^\infty([0, \infty) \times \bar{B}(0, r))$ we have:

$$\int_0^\infty \int_{\bar{B}(0, r)} \left[\frac{\partial \xi}{\partial t}(t, x) - v_t \nabla \xi(t, x) - \lambda \Delta \xi(t, x) \right] \rho_t(x) dx dt = - \int_{\bar{B}(0, r)} \xi(0, x) \rho_0(x) dx.$$

Proof. Our proof is based on the proof of (Bonnotte, 2013) [Theorem 5.6.1]. We proceed in five steps.

(1) Let $h_n \rightarrow 0$ be a sequence given by Theorem S3, such that $\mu_t^{h_n}$ converges to μ_t pointwise. Furthermore we know that μ^{h_n} have densities ρ^{h_n} that converge to ρ in L^r , for $r \geq 1$, and in weak-star topology in L^∞ . Let $\xi \in C_c^\infty([0, \infty) \times \bar{B}(0, r))$. We denote $\xi_k^n(x) = \xi(kh_n, x)$. Using Part 1 of the proof of (Bonnotte, 2013) [Theorem 5.6.1], we obtain:

$$\begin{aligned} \int_{\bar{B}(0, r)} \xi(0, x) \rho_0(x) dx + \int_0^\infty \int_{\bar{B}(0, r)} \frac{\partial \xi}{\partial t}(t, x) \rho_t(x) dx dt \\ = \lim_{n \rightarrow \infty} -h_n \sum_{k=1}^\infty \int_{\bar{B}(0, r)} \xi_k^n(x) \frac{\rho_{kh_n}^{h_n}(x) - \rho_{(k-1)h_n}^{h_n}(x)}{h_n} dx. \end{aligned} \quad (S9)$$

(2) Again, this part is the same as Part 2 of the proof of (Bonnotte, 2013)[Theorem 5.6.1]. For any $\theta \in \mathbb{S}^{d-1}$ we denote by $\psi_{t, \theta}$ the unique Kantorovich potential from $\theta_\#^* \mu_t$ to $\theta_\#^* \nu$, and by $\psi_{t, \theta}^{h_n}$ the unique Kantorovich potential from $\theta_\#^* \mu_t^{h_n}$ to $\theta_\#^* \nu$. Then, by the same reasoning as Part 2 of the proof of (Bonnotte, 2013) [Theorem 5.6.1], we get:

$$\begin{aligned} \int_0^\infty \int_{\bar{B}(0, r)} \int_{\mathbb{S}^{d-1}} \sum_s p_s(\psi'_{s, t, \theta}(\langle \theta, x \rangle)) \langle \theta, \nabla \xi(x, t) \rangle d\theta d\mu_t(x) dt \\ = \lim_{n \rightarrow \infty} h_n \sum_{k=1}^\infty \int_{\bar{B}(0, r)} \int_{\mathbb{S}^{d-1}} \sum_s p_s \psi'_{s, kh_n, \theta}(\theta^*) \langle \theta, \nabla \xi_k^n \rangle d\theta d\mu_{kh_n}^{h_n}. \end{aligned} \quad (S10)$$

(3) Since ξ is compactly supported and smooth, $\Delta \xi$ is Lipschitz, and so for any $t \geq 0$ if we take $k = \lfloor t/h_n \rfloor$ we get $|\Delta \xi_k^n(x) - \Delta \xi(t, x)| \leq Ch_n$ for some constant C . Let $T > 0$ be such that $\xi(t, x) = 0$ for $t > T$. We have:

$$\left| \sum_{k=1}^\infty h_n \int_{\bar{B}(0, r)} \Delta \xi_k^n(x) \rho_{kh_n}^{h_n}(x) dx - \int_0^{+\infty} \int_{\bar{B}(0, r)} \Delta \xi(t, x) \rho_t^{h_n}(x) dx dt \right| \leq CT h_n.$$

On the other hand, we know, that ρ^{h_n} converges to ρ in weak star topology on $L^\infty([0, T] \times \bar{B}(0, r))$, and $\Delta \xi$ is bounded, so:

$$\lim_{n \rightarrow +\infty} \left| \int_0^{+\infty} \int_{\bar{B}(0, r)} \Delta \xi(t, x) \rho_t^{h_n}(x) dx dt - \int_0^{+\infty} \int_{\bar{B}(0, r)} \Delta \xi(t, x) \rho_t(x) dx dt \right| = 0.$$

Combining those two results give:

$$\lim_{n \rightarrow \infty} h_n \sum_{k=1}^\infty \int_{\bar{B}(0, r)} \Delta \xi_k^n(x) \rho_{kh_n}^{h_n}(x) dx = \int_0^{+\infty} \int_{\bar{B}(0, r)} \Delta \xi(t, x) \rho_t(x) dx dt. \quad (S11)$$

(4) Let $\phi_k^{h_n}$ denote the unique Kantorovich potential from $\mu_{kh_n}^{h_n}$ to $\mu_{(k-1)h_n}^{h_n}$. Using Bonnotte, et al. (Bonnotte, 2013) [Propositions 1.5.7 and 5.1.7], as well as Jordan, et al. (Jordan et al., 1998) [Equation (38)] with $\Psi = 0$, and optimality of $\mu_{kh_n}^{h_n}$, we get:

$$\begin{aligned} \frac{1}{h_n} \int_{\bar{B}(0, r)} \langle \nabla \phi_k^{h_n}(x), \nabla \xi_k^n(x) \rangle d\mu_{kh_n}^{h_n}(x) - \int_{\bar{B}(0, r)} \int_{\mathbb{S}^{d-1}} \sum_s p_s(\psi'_{s, kh_n}(\theta^*)) \langle \theta, \nabla \xi_k^n(x) \rangle d\theta d\mu_{kh_n}^{h_n}(x) \\ - \lambda \int_{\bar{B}(0, r)} \Delta \xi_k^n(x) d\mu_{kh_n}^{h_n}(x), \end{aligned} \quad (S12)$$

which is the derivative of $\mathcal{F}_\lambda^{\{\nu_s\}}(\cdot) + \frac{1}{2h_n} \mathcal{W}_2^2(\cdot, \mu_{(k-1)h_n}^{h_n})$ in the direction given by vector field $\nabla \xi_k^n$ is zero.

Let γ be the optimal transport between $\mu_{kh_n}^{h_n}$ and $\mu_{(k-1)h_n}^{h_n}$. Then:

$$\int_{\bar{B}(0, r)} \xi_k^n(x) \frac{\rho_{kh_n}^{h_n}(x) - \rho_{(k-1)h_n}^{h_n}(x)}{h_n} dx = \frac{1}{h_n} \int_{\bar{B}(0, r)} (\xi_k^n(y) - \xi_k^n(x)) d\gamma(x, y), \quad (S13)$$

$$\frac{1}{h_n} \int_{\bar{B}(0, r)} \langle \nabla \phi_k^{h_n}(x), \nabla \xi_k^n(x) \rangle d\mu_{kh_n}^{h_n}(x) = \frac{1}{h_n} \int_{\bar{B}(0, r)} \langle \nabla \xi_k^n(x), y - x \rangle d\gamma(x, y). \quad (S14)$$

Since ξ is C_c^∞ , it has Lipschitz gradient. Let C be twice the Lipschitz constant of $\nabla\xi$. Then we have $|\xi(y) - \xi(x) - \langle \nabla\xi(x), y - x \rangle| \leq C|x - y|^2$, and hence

$$\int_{\bar{B}(0,r)} |\xi_k^n(y) - \xi_k^n(x) - \langle \nabla\xi_k^n(x), y - x \rangle| d\gamma(x, y) \leq C\mathcal{W}_2^2(\mu_{(k-1)h_n}^{h_n}, \mu_{kh_n}^{h_n}). \quad (\text{S15})$$

Combining (S13), (S14) and (S15), we get:

$$\begin{aligned} & \left| \sum_{k=1}^{\infty} h_n \int_{\bar{B}(0,r)} \xi_k^n(x) \frac{\rho_{kh_n}^{h_n} - \rho_{(k-1)h_n}^{h_n}}{h_n} dx + \sum_{k=1}^{\infty} h_n \int_{\bar{B}(0,r)} \langle \nabla\phi_k^{h_n}, \nabla\xi_k^n \rangle d\mu_{kh_n}^{h_n} \right| \\ & \leq C \sum_{k=1}^{\infty} \mathcal{W}_2^2(\mu_{(k-1)h_n}^{h_n}, \mu_{kh_n}^{h_n}). \end{aligned} \quad (\text{S16})$$

As some $\mathcal{F}_\lambda^{\{\nu_s\}}$ have a finite minimum on $\mathcal{P}(\bar{B}(0, r))$, we have:

$$\begin{aligned} \sum_{k=1}^{\infty} \mathcal{W}_2^2(\mu_{(k-1)h_n}^{h_n}, \mu_{kh_n}^{h_n}) & \leq 2h_n \sum_{k=1}^{\infty} \mathcal{F}_\lambda^{\{\nu_s\}}(\mu_{(k-1)h_n}^{h_n}) - \mathcal{F}_\lambda^{\{\nu_s\}}(\mu_{kh_n}^{h_n}) \\ & \leq 2h_n (\mathcal{F}_\lambda^{\{\nu_s\}}(\mu_0) - \min_{\mathcal{P}(\bar{B}(0,r))} \mathcal{F}_\lambda^{\{\nu_s\}}), \end{aligned} \quad (\text{S17})$$

and so the sum on the right hand side of the equation goes to zero as n goes to infinity.

From (S16), (S17) and (S12) we conclude:

$$\begin{aligned} & \lim_{n \rightarrow \infty} -h_n \sum_{k=1}^{\infty} \xi_k^n(x) \frac{\rho_{kh_n}^{h_n} - \rho_{(k-1)h_n}^{h_n}}{h_n} dx = \\ & \lim_{n \rightarrow \infty} \left(h_n \sum_{k=1}^{\infty} \int_{\bar{B}(0,r)} \int_{\mathbb{S}^{d-1}} \sum_s \psi_{s, kh_n, \theta}^{h_n}(\theta^*) \langle \theta, \nabla\xi_k^n \rangle d\theta d\mu_{kh_n}^{h_n} + h_n \sum_{k=1}^{\infty} \int_{\bar{B}(0,r)} \nabla\xi_k^n(x) \rho_{kh_n}^{h_n}(x) dx \right), \end{aligned} \quad (\text{S18})$$

where both limits exist, since the difference of left hand side and right hand side of the equation goes to zero, while the left hand side converges to a finite value by (S9).

(5) Combining (S9), (S10), (S11) and (S18) we get the result. \square

B. Hyperparameters

1. Gaussian Mixture Model parameters:
 - overall number of samples, 6000
 - number of quantiles, 50
 - dimension of input, 2
 - number of samples in training data, 5000
 - step size, 1e-3
 - number of samples in testing data, 1000
 - number of thetas for sliced Wasserstein integration, 256
 - number of epochs, 100
2. Crime Data parameters:
 - overall number of samples, 1994
 - number of quantiles, 50
 - dimension of input, 122
 - number of samples in training data, 1694
 - step size, 1e-2
 - number of samples in testing data, 300
 - number of thetas for sliced Wasserstein integration, 512
 - number of epochs, 200
3. Health Data parameters:
 - overall number of samples, 100000
 - number of quantiles, 50
 - dimension of input, 63
 - number of samples in training data, 70000
 - step size, 1e-2
 - number of samples in testing data, 30000
 - number of thetas for sliced Wasserstein integration, 256
 - number of epochs, 200
4. Adjusted depending on the data set:
 - Autoencoder used within swf:
 - criterion: Defines the loss function as Binary Cross Entropy Loss (`nn.BCELoss()`)
 - optimizer: Uses the Adam optimizer to update the model parameters with a learning rate of 1e-3.

Flags to set in *swf_liouville.py*:

1. `barycenter`: Bool to tell algorithm to use barycenter
2. `fokk_louiville`: Bool to tell algorithm to use the Liouville PDE-based SWF
3. `num_points = Num_samples`
4. `num_dim = input_dim`
5. `batch_size = num_test`

C. Supplementary results

Liouville PDE-based sliced-Wasserstein flow

Table S1. Training and testing losses at convergence for vanilla SWF and Liouville-SWF using the best-performing configurations from the GMM, Crime, and Health datasets. Results are reported as mean \pm standard deviation. For GMM, results are shown without and with the synthetic sensitive attribute. For Crime and Health, results are reported both without and with actual sensitive attributes. Boldface indicates the lower loss or variance within each training or testing comparison.

Data	Sensitive Attribute	SWF training	SWF testing	Liouville-SWF training	Liouville-SWF testing
GMM	–	-26.34 ± 11.29	-26.33 ± 11.54	-27.06 ± 11.52	-26.70 ± 11.55
GMM	2 random	-26.47 ± 11.38	-25.95 ± 10.75	-27.28 ± 11.58	-27.00 ± 11.60
Crime	–	30.91 ± 17.12	31.59 ± 15.82	30.35 ± 16.68	31.17 ± 16.14
Crime	PctRace	31.14 ± 16.87	31.42 ± 15.88	30.38 ± 16.84	31.54 ± 15.85
Health	–	23.41 ± 16.80	23.36 ± 18.06	23.41 ± 16.81	23.29 ± 18.04
Health	AGE	23.30 ± 16.86	23.27 ± 18.10	23.41 ± 16.81	23.29 ± 18.04
Health	sexF	23.26 ± 17.06	23.32 ± 18.05	23.35 ± 16.92	23.32 ± 18.09
Health	totpay	23.35 ± 16.92	23.34 ± 18.09	23.23 ± 16.95	23.21 ± 18.07

Table S2. Comparison of accuracy (MSE) and fairness (KS) between SWF barycenter and Liouville PDE-based SWF across Crime and Health datasets for each sensitive attribute. Boldface indicates the lower MSE or KS in mean values.

Data	Baseline	Sensitive Attributes	λ	Neural ODE Layer Size	MSE	KS
Crime	Liouville PDE-based	PctRace	0.0	32	112.36 ± 13.68	0.0099 ± 0.00045
Crime	SWF barycenter	PctRace	0.0	–	114.28 ± 13.99	0.0096 ± 0.00050
Crime	Liouville PDE-based	PctRace	0.001	32	113.60 ± 13.96	0.0077 ± 0.00029
Crime	SWF barycenter	PctRace	0.001	–	114.43 ± 13.94	0.0058 ± 0.00022
Crime	Liouville PDE-based	PctRace	0.01	32	112.08 ± 13.55	0.0061 ± 0.00037
Crime	SWF barycenter	PctRace	0.01	–	114.00 ± 13.80	0.010 ± 0.00028
Crime	Liouville PDE-based	PctRace	0.1	64	114.73 ± 12.91	0.0084 ± 0.00043
Crime	SWF barycenter	PctRace	0.1	–	115.20 ± 13.16	0.0076 ± 0.00036
Crime	Liouville PDE-based	PctRace	1.0	64	228.67 ± 90.68	0.0089 ± 0.00098
Crime	SWF barycenter	PctRace	1.0	–	234.06 ± 93.12	0.0088 ± 0.0014
Health	Liouville PDE-based	AGE	0.0	64	41.15 ± 9.61	0.0079 ± 0.00067
Health	SWF barycenter	AGE	0.0	–	41.67 ± 10.04	0.0076 ± 0.00030
Health	Liouville PDE-based	AGE	0.001	32	42.39 ± 9.64	0.0068 ± 0.00020
Health	SWF barycenter	AGE	0.001	–	42.96 ± 10.19	0.011 ± 0.00045
Health	Liouville PDE-based	AGE	0.01	32	40.86 ± 9.62	0.0078 ± 0.00038
Health	SWF barycenter	AGE	0.01	–	41.31 ± 9.77	0.0067 ± 0.00056
Health	Liouville PDE-based	AGE	0.1	64	44.00 ± 8.54	0.0070 ± 0.00074
Health	SWF barycenter	AGE	0.1	–	43.66 ± 8.75	0.011 ± 0.00080
Health	Liouville PDE-based	AGE	1.0	128	265.88 ± 190.67	0.0050 ± 0.00051
Health	SWF barycenter	AGE	1.0	–	265.54 ± 191.07	0.0070 ± 0.0015
Health	Liouville PDE-based	sexF	0.0	128	41.91 ± 10.03	0.0093 ± 0.00069
Health	SWF barycenter	sexF	0.0	–	41.79 ± 9.84	0.0098 ± 0.00043
Health	Liouville PDE-based	sexF	0.001	128	41.46 ± 9.74	0.0069 ± 0.00032
Health	SWF barycenter	sexF	0.001	–	41.99 ± 9.68	0.0088 ± 0.00048
Health	Liouville PDE-based	sexF	0.01	32	41.72 ± 9.95	0.0068 ± 0.00039
Health	SWF barycenter	sexF	0.01	–	40.73 ± 9.68	0.0071 ± 0.00074
Health	Liouville PDE-based	sexF	0.1	64	43.23 ± 8.32	0.0073 ± 0.00097
Health	SWF barycenter	sexF	0.1	–	43.77 ± 8.59	0.0083 ± 0.00043
Health	Liouville PDE-based	sexF	1.0	32	265.38 ± 191.87	0.012 ± 0.0024
Health	SWF barycenter	sexF	1.0	–	267.80 ± 192.02	0.011 ± 0.0012
Health	Liouville PDE-based	totpay	0.0	32	42.09 ± 9.71	0.0082 ± 0.0010
Health	SWF barycenter	totpay	0.0	–	40.43 ± 9.38	0.0091 ± 0.00036
Health	Liouville PDE-based	totpay	0.001	32	41.49 ± 9.67	0.0089 ± 0.00053
Health	SWF barycenter	totpay	0.001	–	41.80 ± 9.82	0.012 ± 0.00046
Health	Liouville PDE-based	totpay	0.01	64	41.41 ± 10.18	0.0058 ± 0.00079
Health	SWF barycenter	totpay	0.01	–	42.36 ± 10.08	0.010 ± 0.00047
Health	Liouville PDE-based	totpay	0.1	32	43.60 ± 8.41	0.0084 ± 0.00049
Health	SWF barycenter	totpay	0.1	–	43.56 ± 8.01	0.0060 ± 0.00074
Health	Liouville PDE-based	totpay	1.0	32	265.81 ± 191.23	0.0097 ± 0.00090
Health	SWF barycenter	totpay	1.0	–	264.76 ± 190.79	0.013 ± 0.0019

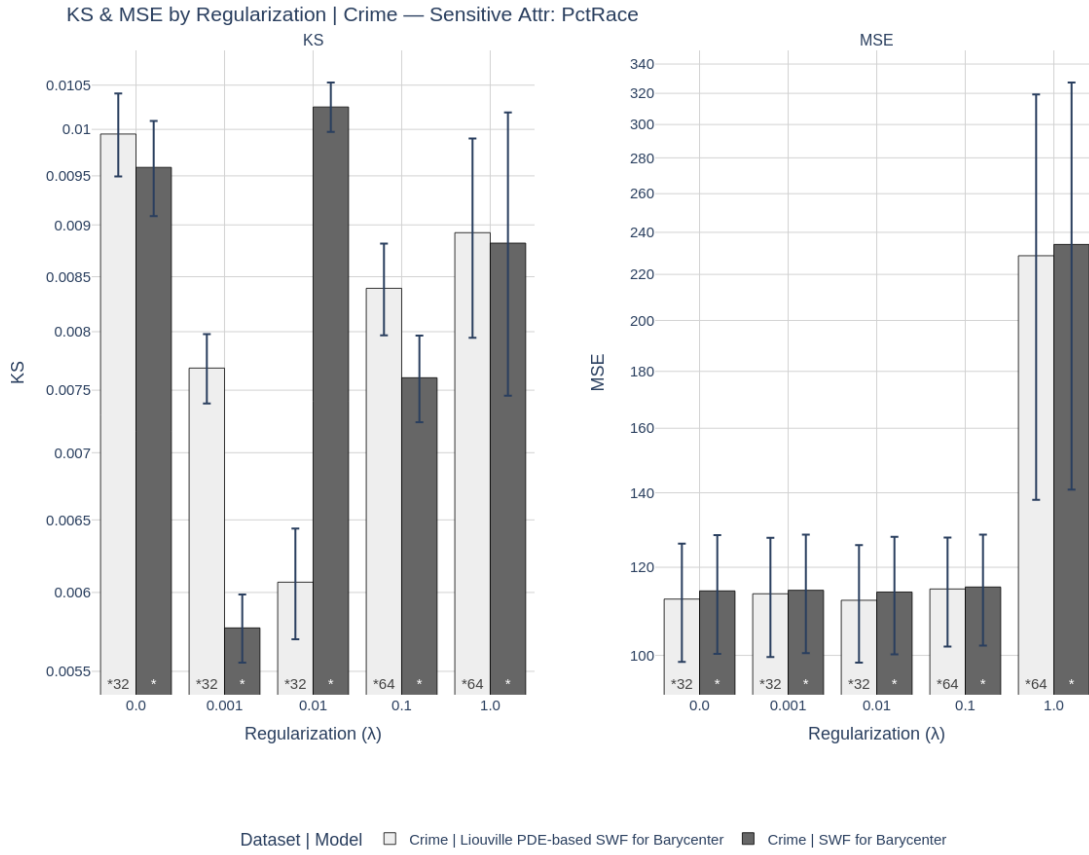


Figure S1. **Crime dataset (PctRace)**. KS (left) and MSE (right) as functions of the regularization parameter λ for Liouville PDE-based SWF barycenter and vanilla SWF barycenter. Error bars denote variability across runs; numbers inside bars indicate the neural ODE layer width.

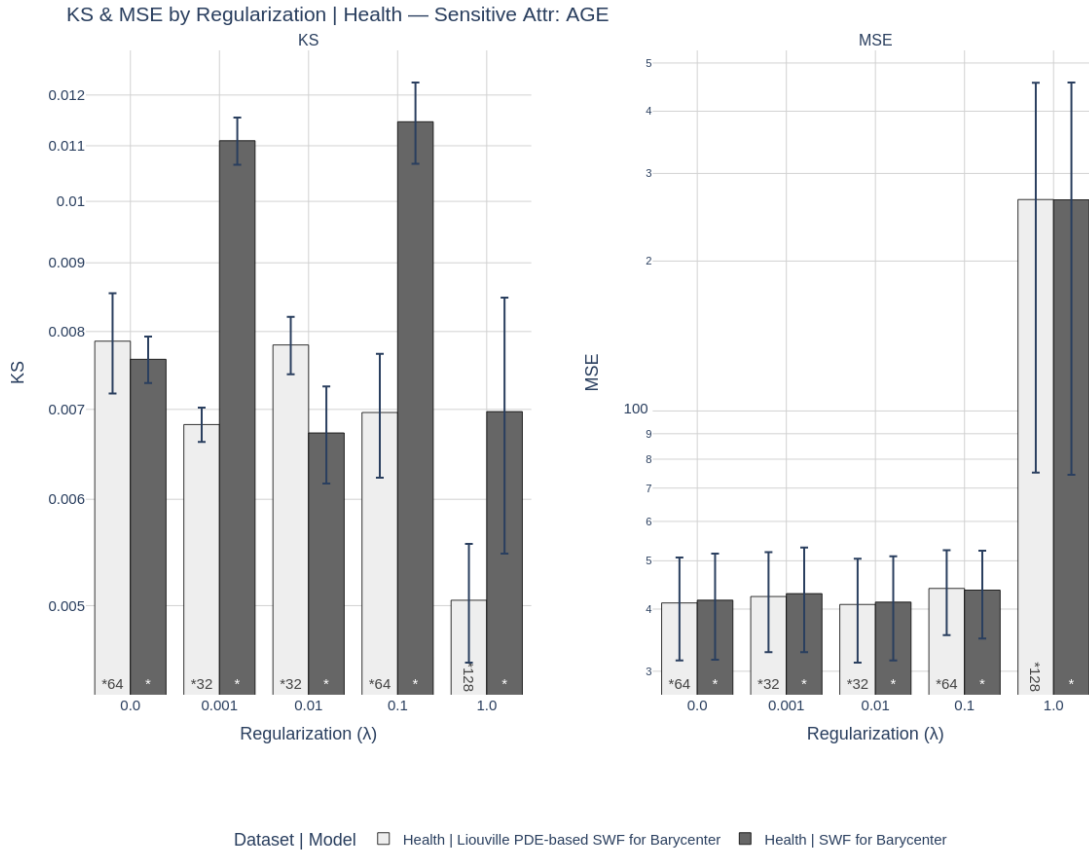


Figure S2. Health Spending dataset on AGE. KS (left) and MSE (right) as functions of the regularization parameter λ under sensitive-attribute conditioning on AGE. Results compare the Liouville PDE-based SWF barycenter and the vanilla SWF barycenter. Error bars indicate variability across runs; numbers inside bars denote the neural ODE layer width.

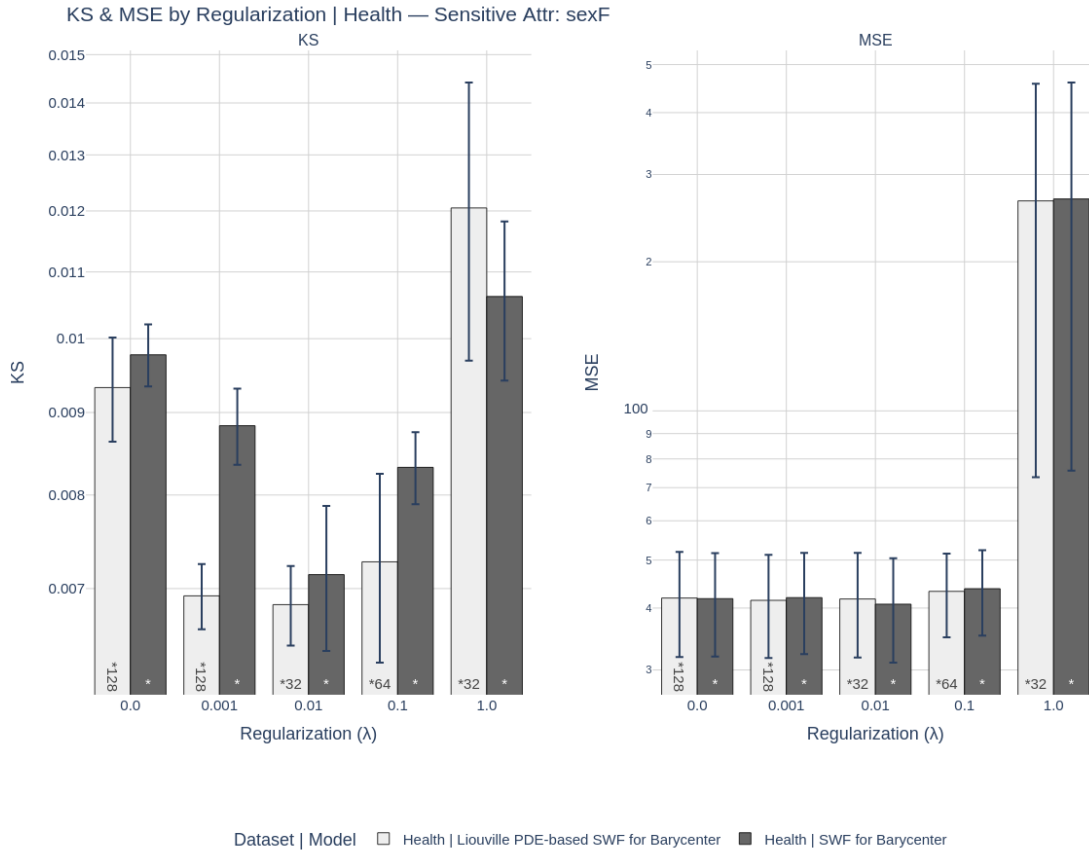


Figure S3. Health Spending dataset on *sexF*. KS (left) and MSE (right) as functions of the regularization parameter λ under sensitive-attribute conditioning on *sexF*. Results compare the Liouville PDE-based SWF barycenter and the vanilla SWF barycenter. Error bars indicate variability across runs; numbers inside bars denote the neural ODE layer width.

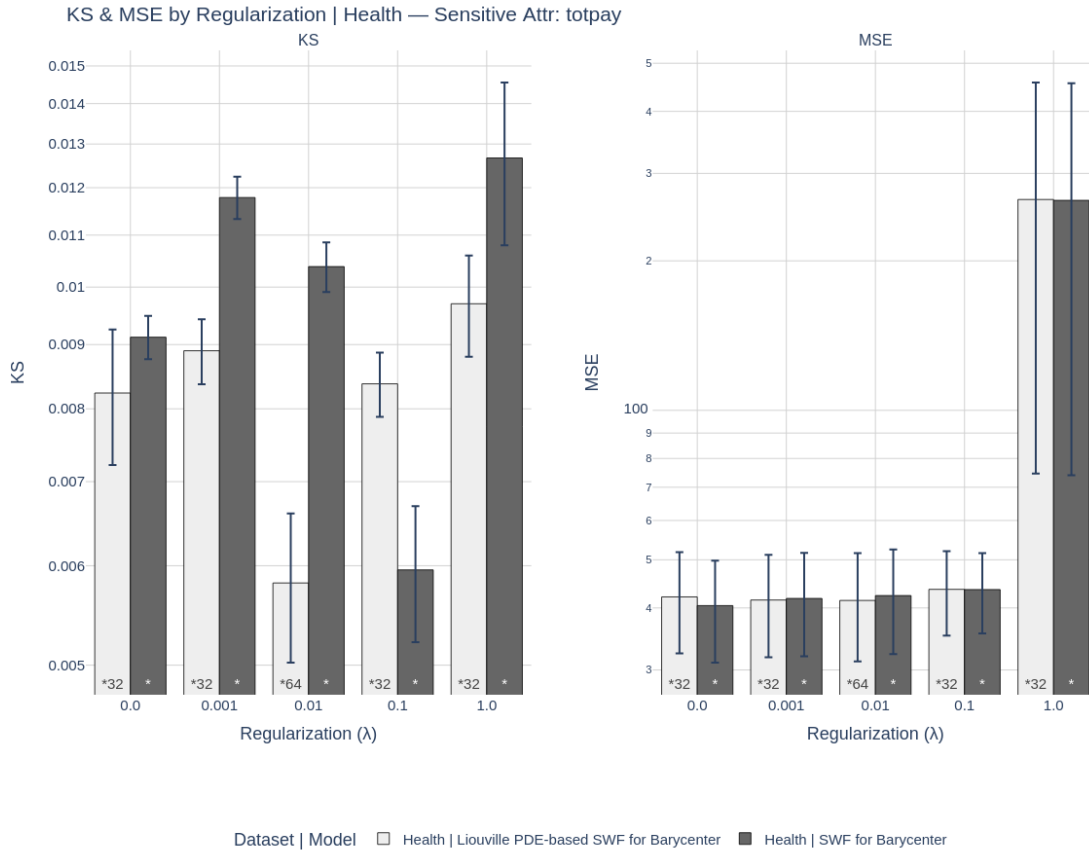


Figure S4. Health Spending dataset on *totpay*. KS (left) and MSE (right) as functions of the regularization parameter λ under sensitive-attribute conditioning on *totpay*. Results compare the Liouville PDE-based SWF barycenter and the vanilla SWF barycenter. Error bars indicate variability across runs; numbers inside bars denote the neural ODE layer width.

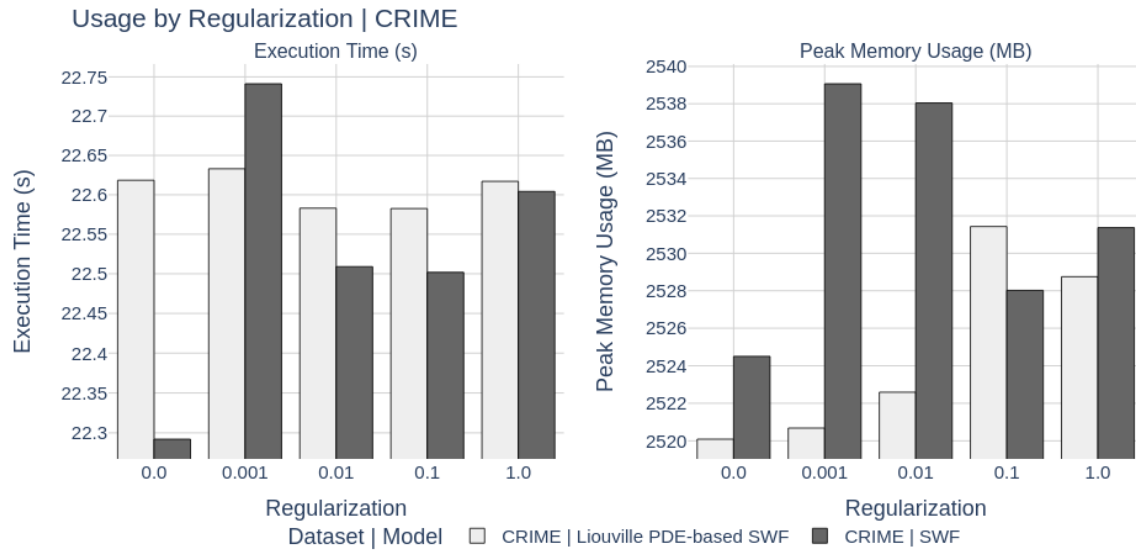


Figure S5. Crime dataset. Execution time (left) and peak memory usage (right) as functions of the regularization parameter λ for the Liouville PDE-based SWF and the vanilla SWF baseline. Across the practical range of regularization values, execution time remains nearly constant and peak memory usage varies only modestly, indicating that PDE-based regularization introduces negligible computational overhead.

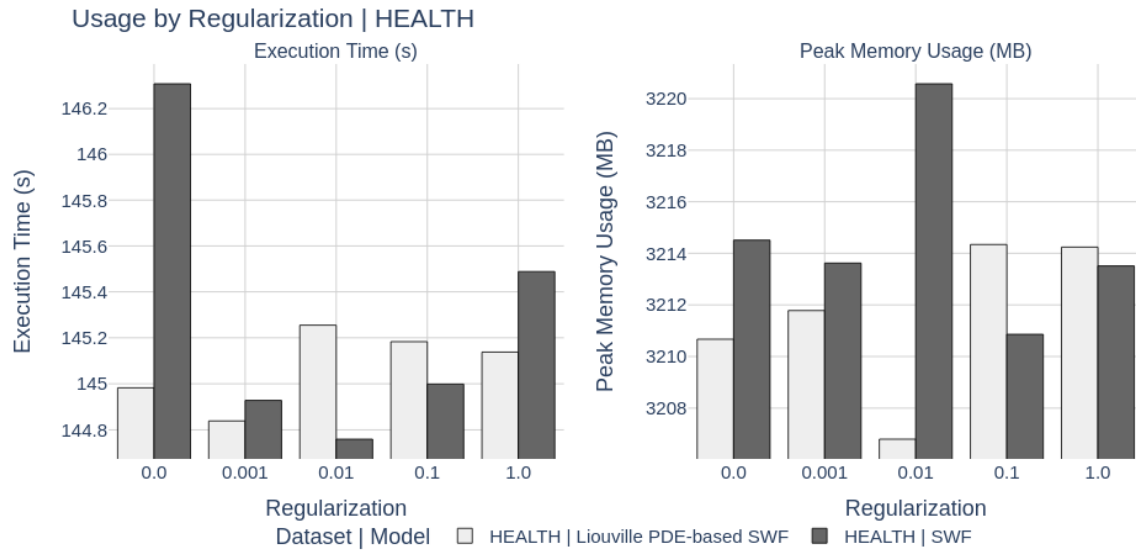


Figure S6. Health Spending dataset. Execution time (left) and peak memory usage (right) as functions of the regularization parameter λ for the Liouville PDE-based SWF and the vanilla SWF baseline. Across the practical range of λ , execution time and memory usage remain stable, with only minor increases at the largest regularization level, confirming the computational scalability of the PDE-based formulation.

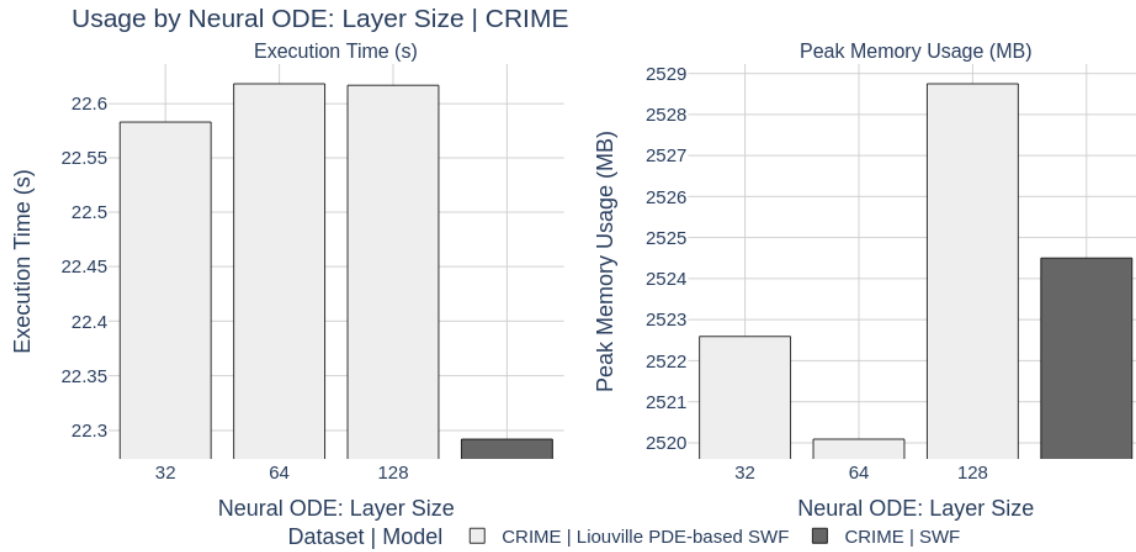


Figure S7. Crime dataset. Execution time (left) and peak memory usage (right) as functions of the neural ODE layer width for the Liouville PDE-based SWF; the vanilla SWF baseline (black bars) does not employ a neural ODE and is therefore shown without an associated layer width. Across configurations, runtime differences remain below 0.2 s and peak memory usage varies by less than 10 MB, indicating that the PDE-based regularization introduces negligible computational overhead.

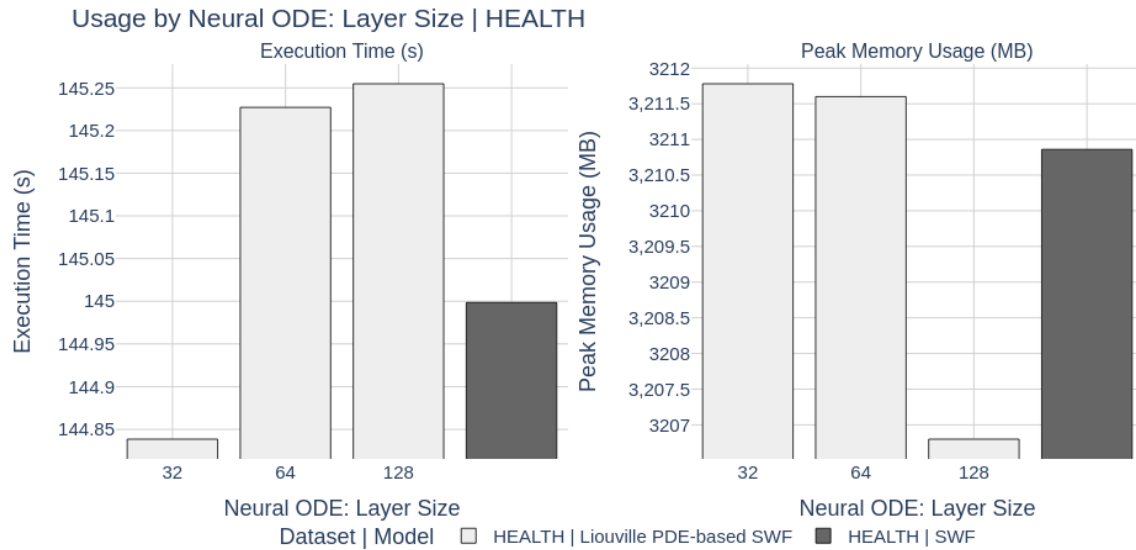


Figure S8. Execution time (left) and peak memory usage (right) as functions of the neural ODE layer width for the Liouville PDE-based SWF; the vanilla SWF baseline (black bars) does not employ a neural ODE and is therefore shown without an associated layer width. Across architectures, runtime differences remain modest (typically below 1 s) and peak memory usage varies by approximately 5–10 MB, indicating that the PDE-based regularization introduces minimal computational overhead.